Mechanism analysis on the mitigation of harbor resonance by periodic undulating topography

Gao, Junliang
School of Naval Architecture and Ocean Engineering, Jiangsu University of Science and Technology

Shi, Huabin
State Key Laboratory of Internet of Things for Smart City and Department of Ocean Science and Technology, University of Macau

Zang, un
Centre for Infrastructure, Geotechnical and Water Engineering (IGWE), Department of Architecture and Civil Engineering, University of Bath

Liu, Yingyi
Research Institute for Applied Mechanics, Kyushu University

出版情報：Ocean Engineering. 281, pp.114923-, 2023-08-01. Elsevier
バージョン：
権利関係：

Mechanism analysis on the mitigation of harbor resonance by periodic undulating topography

Junliang Gao [a, b, c], Huabin Shi [b *], Jun Zang [d], Yingyi Liu [e]

[a] *School of Naval Architecture and Ocean Engineering, Jiangsu University of Science and Technology, Zhenjiang 212100, China*

[b] *State Key Laboratory of Internet of Things for Smart City and Department of Ocean Science and Technology, University of Macau, Macao 999078, China*

[c] *Key Laboratory of Water Security Guarantee in Guangdong-Hong Kong-Marco Greater Bay Area of Ministry of Water Resources, Guangzhou 510611, China*

[d] *Centre for Infrastructure, Geotechnical and Water Engineering (IGWE), Department of Architecture and Civil Engineering, University of Bath, BA2 7AY, U.K.*

[e] *Research Institute for Applied Mechanics, Kyushu University, Fukuoka, Kasuga, 816-8580, Japan*

Abstract:

Gao et al. (2021. Investigation on the effects of Bragg reflection on harbor oscillations. Coastal Engineering, 170: 103977) attempted to utilize Bragg reflection to alleviate harbor resonance, and discovered its significant effectiveness for the first time. The Bragg reflection occurred over periodic topographies deployed outside and parallel to the harbor entrance. However, the inherent mitigating mechanisms were not revealed. In this paper, the Bragg reflection over a patch of sinusoidal bars and its coupling effects with the harbor are studied using a Boussinesq-type model. Different from the previous study, the sinusoidal bars with various numbers and amplitudes are arranged in the manner of an arc layout around rather than parallel to the entrance. A physical process decomposition method is proposed to reveal the inherent mitigation mechanism. Moreover, the condition under which harbor resonance is not excited by incident waves (hereinafter referred to as "harbor non-resonance condition") is also investigated, and the similarities/differences of mitigation mechanisms between the harbor resonance and non-resonance conditions are discussed. Finally, for the harbor resonance condition, the effects of the number and the amplitude of sinus-

Email: gaojunliang880917@163.com (J. Gao)

[*] Corresponding author: HuabinShi@um.edu.mo (H. Shi)

oidal bars on the best mitigation effect and optimal bar wavelength, which can attain the best mitigation effect, are systematically analyzed.

Keywords:
Harbor resonance; Long-period waves; Bragg reflection; Sinusoidal bars; Numerical simulation; FUNWAVE 2.0 model

1. Introduction

Harbor resonance (also termed *seiches* or *harbor oscillations*) refers to the long-period resonance phenomenon of the water body inside the bay or the harbor (intuitively reflected in the trapping and sharp amplification of long-period wave energy). It may be excited by various external forces, such as shear flows (Fabrikant, 1995), seisms (Zheng et al., 2021; Zheng et al., 2022), infragravity waves (Gao et al., 2016; Mahmoudof et al., 2021; Mahmoudof and Siadatmousavi, 2020; Priya et al., 2023), tsunami waves (Gao et al., 2021a; Kulikov et al., 1996; Ma et al., 2021; Rupali et al., 2020), wave groups (Gao et al., 2020; Mei and Agnon, 1989), atmospheric fluctuations (De Jong and Battjes, 2004; Sun and Niu, 2021), the landsilde-generated impact waves (Dong et al., 2010a) and the local water surface disturbance (Gao et al., 2023; Gao et al., 2018b). Significant motions of the ships moored in the harbor may be caused by the harbor resonance phenomenon, which would disturb the operation of docks, and even produce excessive mooring forces and eventually break mooring lines (Gulshan et al., 2020; Kumar et al., 2016; Sakakibara and Kubo, 2008). Harbor resonance could also result in remarkable overtopping and inundation near quays (Maravelakis et al., 2021). The related studies on harbor resonance at the early stage and in the last three decades have been well summarized by Miles (1974) and Rabinovich (2009), respectively.

This phenomenon has been a concern for the coastal engineering community since the 1940s (Knapp and Vanoni, 1945). To understand the generation mechanism and the resonance characteristics, numerous analytical investigations on the resonance of the harbor with relatively simple plane shapes and topographies have been performed (e.g., Liu (1986); Wang et al. (2015); Wang et al. (2014)). A few physical experiments have been conducted to investigate the generation mechanisms or the resonance characteristics (e.g., Dong et al. (2020); Lee (1971); Ma et al. (2021);

Sammartino et al. (2014)). Meanwhile, various numerical models have also been established to study this hydrodynamic phenomenon, among which Boussinesq-type equation models are the most widely used (e.g., Gao et al. (2017); Gao et al. (2019); Kaur et al. (2022); Malej et al. (2021); Shao et al. (2023); Zheng et al. (2021)). Besides, various mild-slope equation models have also been applied to study harbor resonance (e.g., Chen et al. (2006); Dong et al. (2023); Zhao et al. (2014)). However, compared to the Boussinesq-type models, the mild-slope equation models are still not ideal in simulating this phenomenon due to nonlinear wave-wave ineraction in shallow water (Dong et al., 2022).

How to effectively alleviate this adverse hydrodynamic phenomenon has always been problematic in coastal engineering. Heretofore, the overwhelming majority of investigations on mitigating harbor resonance were implemented from the following three aspects. The first aspect is to change the plane layout of the harbor. A significant change in the harbor layout may remarkably vary the eigen-periods of the harbor and lead to a substantial difference between the eigen-periods of the reconstructed/expanded harbor and the periods of the original offshore incident waves that can excite harbor resonance. For the built harbors, the change of their plane layouts is realized by deploying new breakwaters (Lee and Xing, 2009; Maa et al., 2011). The second aspect is to reduce the reflectivity of the wharf to the long-period waves. The essence of the harbor resonance phenomenon lies in that the long-period waves form standing waves inside the harbor, and one of the nodal lines is just located nearby the harbor entrance. Therefore, if the reflectivity of long-period waves on the wharf could be reduced, their amplification inside the harbor can be effectively suppressed (Gonzalez-Escriva et al., 2020; Isaacson and Qu, 1990; Zhao et al., 2022). The third aspect is to adopt permeable breakwaters. By arranging breakwaters with a certain degree of permeability, the long-period wave energy can be released into the open sea via the harbor entrance and the breakwater body (Yu and Chwang, 1994).

However, for a built harbor, all of the above-mentioned measures require a large-scale reconstruction or expansion of the harbor, such as creating new breakwaters to significantly change the plane layout, transforming the wharf into a structural form to better absorb long-period waves, or transforming the impermeable breakwater into a permeable breakwater. The cost of all these measures is exceptionally high and even infeasible (Lee and Xing, 2009; Leys et al., 2018).

The propagation and scatter of water waves over periodic undulating topographies have been

studied in the last few decades, among which the most attractive phenomenon is the well-known Bragg resonant reflection (e.g., Alam et al. (2010); Davies (1982); Kar et al. (2020); Liu (2023); Liu et al. (2022c); Peng et al. (2022); Xu et al. (2023)). When the surface wavelength is about twice the topographic wavelength, the incoming waves would be significantly reflected by the periodic bottom, and only a small part of the wave energy can be transmitted to the coastline. It is shown in Bragg reflection that periodic topographies offshore may significantly inhibit the propagation of the incoming energetic waves toward the shoreline and secure the coast from attack (Fan et al., 2021; Guo et al., 2021; Liu et al., 2022a; Liu et al., 2022b; Ni and Teng, 2021a; Ning et al., 2022; Pan et al., 2022; Xie, 2022; Xie and Liu, 2023).

Because periodic undulating topographies are commonly observed near harbors (e.g., Araújo et al. (2004); Dodd et al. (2003); Russell (1982)), Gao et al. (2021b) adopted a fully nonlinear Boussinesq model to explore and confirm the possibility of utilizing the Bragg reflection phenomenon to alleviate harbor resonance for the first time. In the paper, an elongated harbor was considered, and sinusoidal bars with different numbers and amplitudes were arranged outside the harbor and parallel to the harbor entrance. Compared with the previous three mitigation measures, this potential new method has two significant advantages. First, for the built harbor, it does not require modifying the existing plane layout and structural form. Second, the principle of alleviating harbor resonance by significantly preventing long-period wave energy from penetrating the harbor has universal applicability.

Although the feasibility of alleviating harbor resonance by utilizing the Bragg reflection has been proved by Gao et al. (2021b), the inherent mitigation mechanism was not fully revealed therein. Instead, only a possible reason was proposed, which is described as follows (refer to Fig. 1). The offshore incident waves propagate normally over the sinusoidal bars. It is the perfect condition to produce Bragg resonant reflection, which would cause minimal incident waves that can pass through the bars and enter the harbor. On the contrary, the radiated waves are mostly cylindrical concerning the harbor entrance. They propagate along various directions and are not in the optimal condition for Bragg resonant reflection. In addition, the overwhelming majority of the reflected waves of the radiated waves by the periodic undulating topographies do not propagate directly back into the harbor but attack the surrounding coastline. Therefore, as a whole, the alleviating effect of the bars resulting from the remarkable reflection of the incident waves is stronger

than its aggravating effect caused by the reflection of the radiated waves back into the harbor.

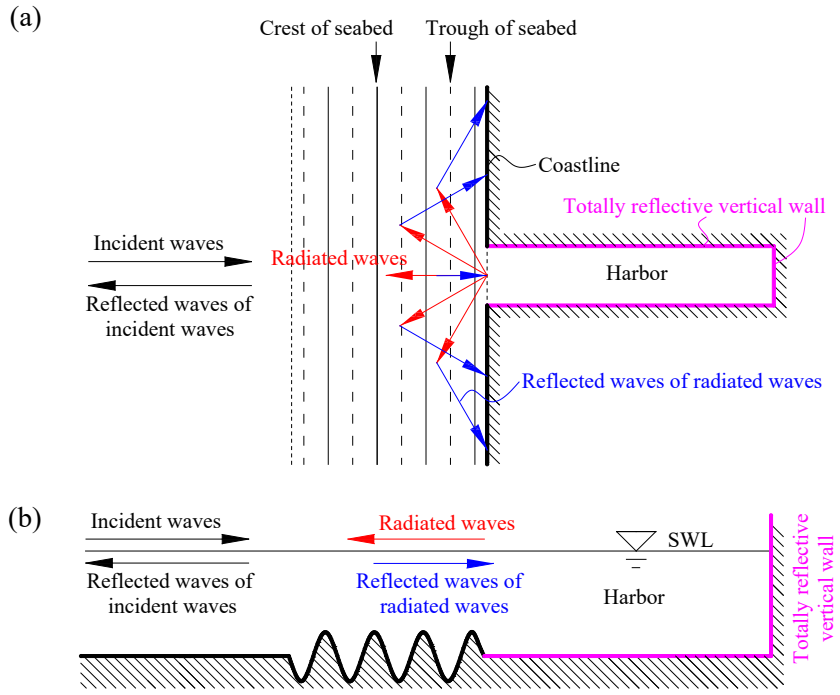

Fig. 1. Schematic diagram for the wave propagation process to explain the possible mitigation mechanism proposed by Gao et al. (2021b): (a) the top view, (b) the front view of the cross-section along the central axis of the harbor

Based on the knowledge of the Bragg reflection and the wave radiation and diffraction, it can be judged that the possible reason mentioned above is reasonable. However, there are still some questions to be answered, that is,

Question (1): Is the possible reason mentioned above the only mechanism for periodic undulating topographies to effectively mitigate harbor resonance?

Question (2): If the answer to Question (1) is no, is the possible reason the most essential mitigation mechanism? If not, what is the most critical mechanism?

Question (3): In Gao et al. (2021b), only the influences of Bragg reflection on the harbor resonance condition were investigated. How Bragg reflection affects the harbor non-resonance condition is still unknown. For the harbor non-resonance condition, if Bragg reflection could also effectively alleviate the long waves inside the harbor, what are the similarities and differences of the influence characteristics of Bragg reflection on the long waves inside the harbor under both the

harbor resonance and non-resonance conditions? Further, what are the internal mechanisms for the different influence characteristics if they exist?

From the perspective of taking Bragg reflection as a potential measure to alleviate harbor resonance, the answers to Questions (1) and (2) are vitally important because they would fully reveal the coupling mechanisms between harbor resonance and the periodic topography outside and provide a solid theoretical basis for possible practical engineering applications in the future. As for Question (3), although the harbor non-resonance condition does not pose a threat to the efficiency of loading/unloading operation and the safe of the mooring ship inside the harbor, finding out its answer will help us to understand the coupling mechanism between the harbor and the periodic topography more comprehensively.

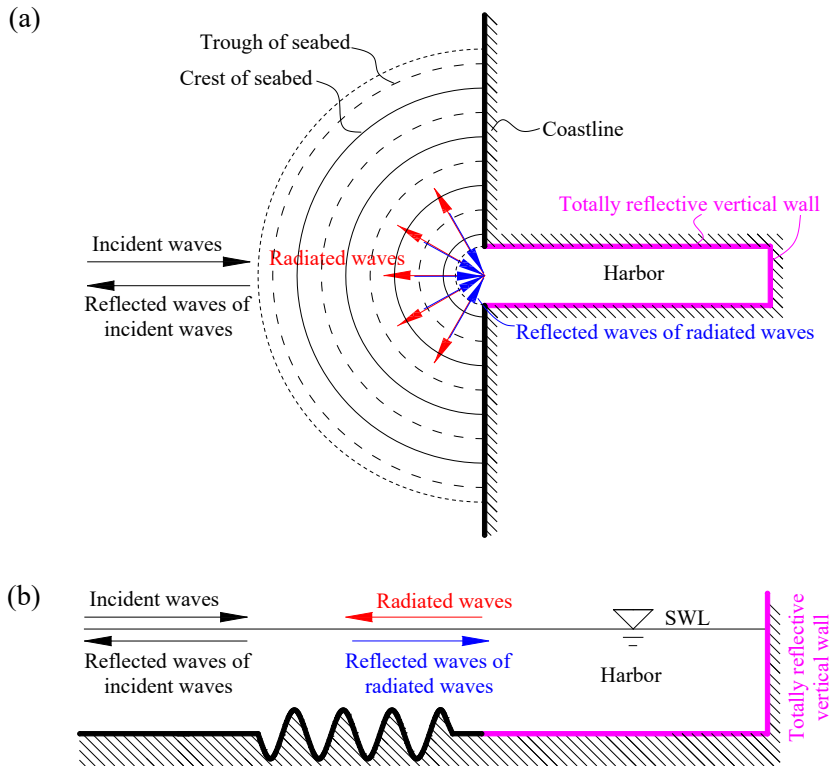

Fig. 2. Schematic diagram of the wave propagation process for the interaction between the harbor and a patch of arc-shaped sinusoidal bars outside: (a) the top view, (b) the front view of the cross-section along the central axis of the harbor

To answer Question (1), this paper will also study the interactions between the incident long monochromatic waves, a patch of sinusoidal bars, and a harbor. However, different from Gao et al.

(2021b), the sinusoidal bars with various numbers and amplitudes will be arranged outside the harbor in a manner of the arc layout around the entrance (see Fig. 2). For this case, although the radiated waves are still mostly cylindrical concerning the entrance, they would always propagate perpendicularly with the bars in all directions, which conform to the optimal condition for Bragg reflection. Furthermore, most of the reflected waves of the radiated waves by the bars would propagate directly back into the harbor. These two factors can significantly hinder the leakage of long-period wave energy into the open sea. If the arc-shaped bars could still alleviate harbor resonance effectively, it would mean that there exist other unknown mitigation mechanisms.

Furthermore, from the perspective of practical engineering, the arc-shaped bars may have an advantage over the parallel bars. Considering that the incident waves outside harbors usually come from various directions, the arc-shaped bars can play an equally good blockage effect for them. Then they may effectively mitigate the harbor resonance excited by the incident waves in any direction.

To answer Question (2), an ingenious physical process decomposition method will be proposed (explained in detail in Section 3). To answer Question (3), the harbor resonance and the non-resonance conditions will be considered in the present study. Moreover, if the capability of the arc-shaped bars to alleviate harbor resonance was proved in this article, one more question would need to be further answered, that is:

Question (4): How are the best mitigation effect and its corresponding optimal bar wavelength influenced by the bar parameter variations (including the amplitude and the number)?

The remainder of the article will focus on solving the above four questions and is organized as follows. Section 2 introduces the numerical model adopted, and its capability to reproduce the Bragg reflection triggered by incident waves with various directions is examined by an existing analytical solution. Section 3 illustrates the specific principle of the physical process decomposition method. Section 4 describes the incident wave parameters and the numerical wave tank in detail. The research results and explanations are presented in Section 5. Finally, conclusions are drawn in Section 6.

2. Numerical model

2.1. Numerical model description

All simulations in this paper are performed by adopting a widely-used Boussinesq model, FUNWAVE 2.0, developed by Kirby et al. (2003). The fully nonlinear Boussinesq equations of Wei et al. (1995) are discretized and solved by the finite difference scheme, and the control equations are formulated as

$$\eta_t + \nabla \cdot \mathbf{M} = 0, \tag{1}$$

and

$$\mathbf{u}_{\alpha t} + (\mathbf{u}_\alpha \cdot \nabla)\mathbf{u}_\alpha + g\nabla\eta + \mathbf{V}_1 + \mathbf{V}_2 = 0, \tag{2}$$

in which

$$\mathbf{M} = (h+\eta)\mathbf{u}_\alpha + (h+\eta)\cdot\left[\frac{z_\alpha^2}{2} - \frac{1}{6}(h^2 - h\eta + \eta^2)\right]\nabla(\nabla\cdot\mathbf{u}_\alpha) + (h+\eta)\left[z_\alpha + \frac{1}{2}(h-\eta)\right]\nabla\left[\nabla\cdot(h\mathbf{u}_\alpha)\right], \tag{3}$$

$$\mathbf{V}_1 = \frac{z_\alpha^2}{2}\nabla(\nabla\cdot\mathbf{u}_{\alpha t}) + z_\alpha\nabla\left[\nabla\cdot(h\mathbf{u}_{\alpha t})\right] - \nabla\left[\frac{1}{2}\eta^2\nabla\cdot\mathbf{u}_{\alpha t} + \eta\nabla\cdot(h\mathbf{u}_{\alpha t})\right], \tag{4}$$

$$\mathbf{V}_2 = \nabla\left[(z_\alpha - \eta)(\mathbf{u}_\alpha\cdot\nabla)(\nabla\cdot(h\mathbf{u}_\alpha)) + \frac{1}{2}(z_\alpha^2 - \eta^2)(\mathbf{u}_\alpha\cdot\nabla)(\nabla\cdot\mathbf{u}_\alpha)\right] + \frac{1}{2}\nabla\left[(\nabla\cdot(h\mathbf{u}_\alpha) + \eta\nabla\cdot\mathbf{u}_\alpha)^2\right]. \tag{5}$$

t, η, h, and g refer to the time, the wave elevation, the water depth, and the gravitational acceleration, respectively. $\nabla=(\partial/\partial x, \partial/\partial y)$ and $\mathbf{u}_\alpha$ refer to the vector of horizontal gradient and that of horizontal velocity at $z_\alpha=\alpha h$, respectively. In the present study, α is set to −0.531 to achieve the best dispersion performance of the control equations (Wei et al., 1995).

The numerical model adopts the one-way wave-making technique proposed by Chawla and Kirby (2000) to produce various desired waves (including monochromatic and random waves). The so-called "one-way" wave generation means that the generated waves propagate only to one side of the wave-making zone. This technique achieves the one-way wave generation by adding a symmetric source term and an anti-symmetric one concerning the centerline of the wave-making zone to the continuity equation and momentum equation. The characteristic of the one-way wave generation in the numerical model provides an essential basis for the physical process decomposition method described in Section 3. The "sponge layer" following Wei et al. (1995) is adopted and deployed at the boundaries of the computational domain to absorb outgoing waves effectively. With considerable ameliorations in dispersive and nonlinear performances, the FUNWAVE 2.0

model is accurate and robust in simulating the propagation of waves from medium to shallow water depth (Bruno et al., 2009; Gao et al., 2018a).

2.2. Numerical model verification

There is no direct experimental or analytical study on the coupling between periodic undulating topographies and harbors. However, because the complete physical process shown in Fig. 2 mainly includes two main sub-processes (i.e., the interaction between incident waves and the sinusoidal bars and the interaction between waves and the harbor), the model's capability can be verified by separately reproducing Bragg reflection and harbor resonance. For producing harbor resonance, its ability has been thoroughly examined in literature (e.g., Dong et al. (2010b); Ma et al. (2020)). Hence, only the performance of the numerical model in producing Bragg reflection is tested here. In fact, the capacity of the numerical model to reproduce the Bragg resonance reflection has been partially validated in Gao et al. (2021b). However, only the condition that the direction of the incident waves is normal to the sinusoidal bars was examined therein. This subsection is an extension and supplement to the model verification implemented by Gao et al. (2021b).

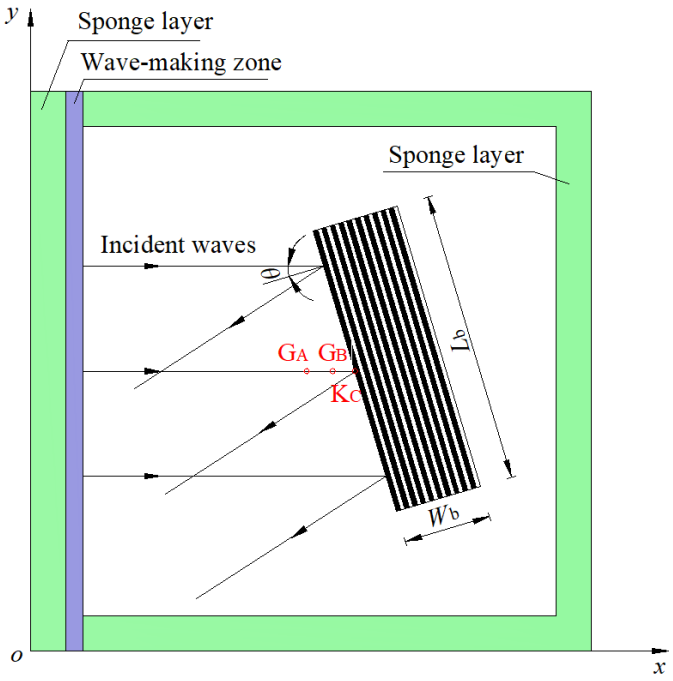

Fig. 3. Top view of the numerical wave tank (NWT) for the interactions between incident waves and a patch of parallel sinusoidal bars with various relative angles.

The analytical solution or experimental data for Bragg reflection over arc-shaped/circular periodic topographies have not yet been reported. However, the arc-shaped periodic topography can be regarded as a synthetic topography consisting of infinitely short straight segments with various direction angles. Therefore, an equivalent testing scheme is to simulate the Bragg reflection over the parallel periodic bottom subjected to oblique incident waves, for which an analytical study has been carried out by Mei et al. (1988).

The sketch for the interactions between the incident waves and a patch of parallel sinusoidal bars with various angles is illustrated in Fig. 3. The angle between the propagation direction of the incident waves and the normal direction of the bars is defined as θ. Based on the perturbation theory, the analytical solution for the reflection coefficient R has been derived by Mei et al. (1988) and is formulated as

$$R(\theta)=\frac{\Omega_0 i\sinh(PW_{\mathrm{b}})\cos 2\theta}{\cos\theta\left[iPC_g\cosh(PW_{\mathrm{b}})+\Omega\cos\theta\sinh(PW_{\mathrm{b}})\right]} \tag{6}$$

when the detuning frequency Ω is smaller than the cutoff frequency $\Omega_0\left|\frac{\cos 2\theta}{\cos^2\theta}\right|$. In the above equation, Ω_0 is expressed as

$$\Omega_0=\frac{\omega kD}{2\sinh(2kh_0)}, \tag{7}$$

in which ω and k respectively denote the angular frequency and the wavenumber of the incident waves, D denotes the bar amplitude, i denotes the imaginary unit, C_g denotes the group velocity of incident waves, h_0 denotes the average constant water depth, W_{b} is the width of the patch, and P is formulated as

$$P=\frac{\Omega_0\cos\theta}{C_g}\left[\left(\frac{\cos 2\theta}{\cos^2\theta}\right)^2-\left(\frac{\Omega}{\Omega_0}\right)^2\right]^{1/2} . \tag{8}$$

In this section, only the so-called "perfect tuning" resonance condition is considered, and the detuning frequency Ω of the incident waves under this condition is always equal to zero. The following geometric relationship needs to be satisfied to achieve the perfect tuning resonance, i.e.,

$$k=k_{\mathrm{b}}/(2\cos\theta), \tag{9}$$

where k_{b} denotes the wavenumber of the sinusoidal bars.

A series of cases are simulated using the numerical model. The dimensions of the domain shown in Fig. 3 are 26 m ×26 m. The wave-making zone with a width of 0.25 times the incident

wavelength is arranged inside the domain to generate the incident monochromatic waves. The sponge layers with a width of 2 m are deployed at all four boundaries of the domain to dissipate the outgoing waves effectively. In all cases, the direction of the incident waves keeps unchanged and always follows the positive direction of the x-axis. At the same time, their wavenumber, k, changes from case to case to meet the perfect tuning resonance condition expressed by Eq. (9). The patch of bars is rotated around the central point of its left boundary (i.e., point K_C) so that the normal direction of the bars is gradually changed. Different from k, the bar wavenumber, k_b, keeps a constant value. The geometric parameters for the patch of bars and the water depth are set according to Mei et al. (1988). Their specific values are listed in Table 1, where $S=2\pi/k_b$ and N denote the wavelength and the number of bars, respectively.

Table 1. Specific values for the geometric parameters of the bar patch, the water depth, and the coordinates of G_A, G_B, and K_C.

S (m)	D (m)	N	L_b (m)	W_b (m)	θ (°)	h_0 (m)	Coordinates (m, m)		
							G_A	G_B	K_C
0.5	0.0247	10	16	5	0-55	0.154	(12.15, 13)	(12.35, 13)	(13, 13)

The analytical solution of Mei et al. (1988) aims at a patch of parallel sinusoidal bars with an infinite length. However, considering that the space of the computational domain is limited, the length of the patch, L_b, is set to a limited value of 16 m. In all cases, the incident wave steepness ka keeps 0.05, where a is the amplitude of the incident waves. Two wave gauges (i.e., G_A and G_B) are deployed near the left boundary of the patch to record the time histories of the wave elevations. Based on their records and the wave analysis technique proposed by Goda and Suzuki (1976), the reflection coefficient of the bars can be evaluated. The coordinates of the two gauges and the point K_C are presented in Table 1. The uniform grid size of $\Delta x=\Delta y=0.025$ m and the time step of $\Delta t=0.01$ s are adopted. In each case, the total time of 40 wave periods is simulated. The time histories of the wave elevations in the last 20 wave periods are used to calculate the reflection coefficient.

Fig. 4 compares the present model's reflection coefficients and Mei et al.'s (1988) theoretical predictions. Moreover, the reflection coefficients obtained by a High-Order Spectral (HOS) numeral model in Hao et al. (2022) are presented. Overall, the present numerical results coincide

quite well with both the theoretical prediction and the HOS-based numerical data. In addition, compared to the HOS-based results, the ones obtained by the present model seem closer to the analytical solution.

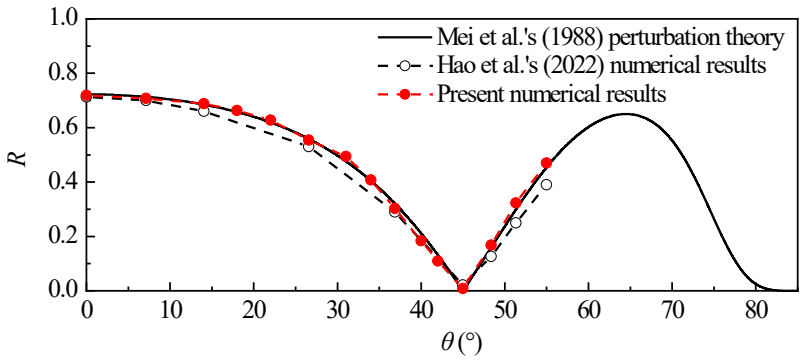

Fig. 4. Comparisons of the present simulated reflection coefficients with both the theoretical solution of Mei et al. (1988) and the High-Order Spectral (HOS) based numerical results of Hao et al. (2022).

3. Physical process decomposition method

To deeply reveal the influence mechanism of the periodic undulating topography on the wave condition inside the harbor under actions of the incident long waves, an ingenious physical process decomposition method is proposed in this section. Its schematic diagram is illustrated in Fig. 5. In theory, the actual influences of the periodic topography on the harbor depend on the relative influence strength of the former on the following two sub-processes: (1) the transmission sub-process and (2) the radiation sub-process. Hence, the complete physical process shown in Fig. 5a is decomposed into these two sub-processes.

The effect of the periodic topography on the transmission sub-process is first investigated (see Fig. 5b and d). Suppose Bragg resonant reflection occurs over the periodic topography. In such a case, most of the incident wave energy from the open sea can be reflected, and only a tiny proportion of the incident wave energy can propagate into the harbor. Under this condition, the periodic topography outside the harbor could significantly reduce the wave energy inside the harbor. The critical issue here lies in how to quantitatively determine the attenuation rate of the waves inside the harbor caused by the transmission blockage described above. If the incident monochromatic waves with a specific frequency had a minimal amplitude, they would be amplified by the

harbor with a particular amplification factor. In other words, the harbor is like a linear signal amplifier for the incident waves with the same frequency but different amplitudes. The signal amplifier will magnify the incident waves with an identical amplification factor as long as their amplitudes are small. Hence, the attenuation rate of the waves inside the harbor in the complete physical process caused by the bars is equal to that of the transmitted waves. Via designing a transmission group shown in Fig. 5b and a corresponding control group in Fig. 5d where the bar does not exist, the attenuation rate of the transmitted waves (denoted by K_T hereinafter) can be easily calculated.

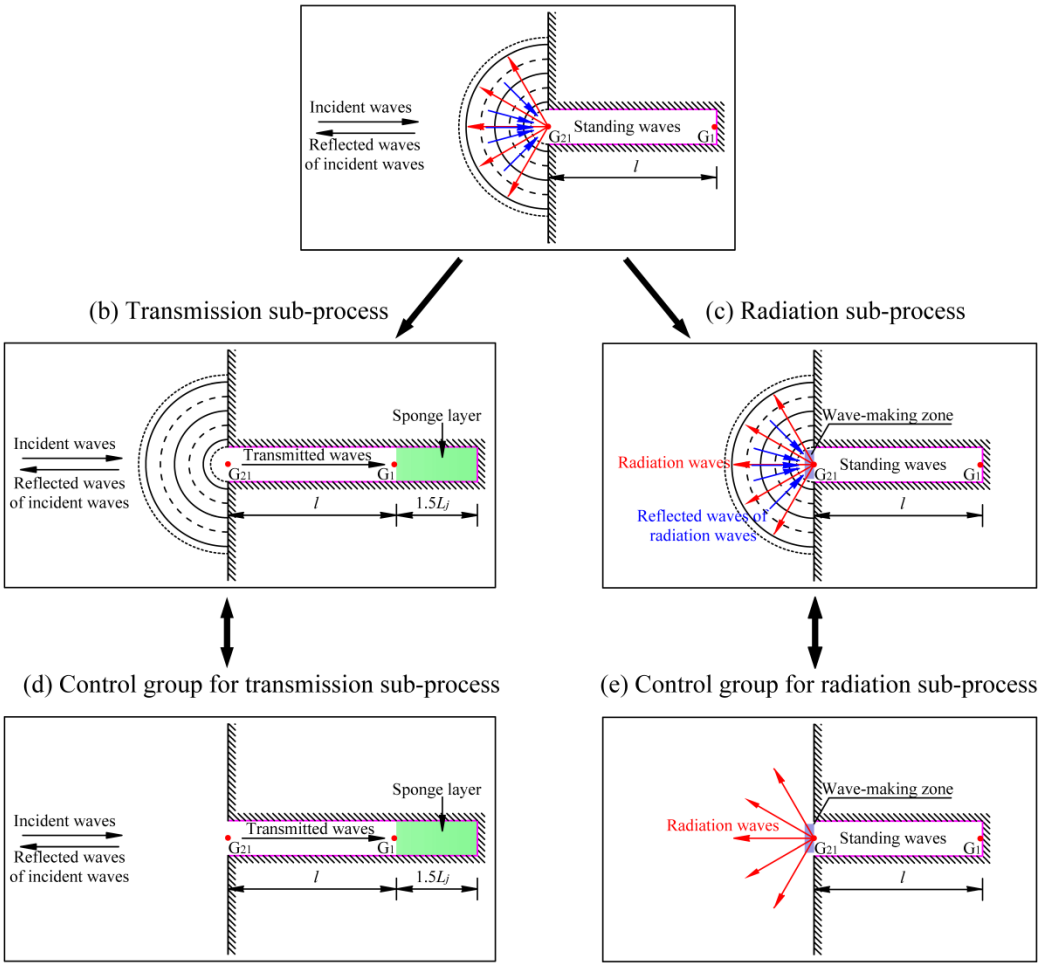

Fig. 5. Schematic diagram for the physical process decomposition method. The meanings of all the symbols and variables in the figure will be explained in Section 4.

Then, the influence of the periodic topography on the radiation sub-process is studied (see Fig. 5c and e). Due to the fully reflective backwall, standing waves are always formed inside the harbor. These standing waves release their energy into the open sea in the form of radiation waves

via the harbor entrance. Bragg resonant reflection over the arc-shaped bars can also significantly hinder the release of wave energy into the open sea, which would cause the significant growth of the wave energy inside the harbor. To quantitatively estimate its growth rate, the incident monochromatic waves are no longer generated in the open sea. Instead, a wave-making zone with a width equal to the width of the harbor is arranged just outside the entrance. Because the one-way wave-making technique is adopted (the waves made by the wave-making zone propagate only along the positive direction of the x-axis), the standing waves are formed inside the harbor. The radiation sub-process for the complete physical process can be perfectly reproduced. Considering again that the harbor acts like a linear signal amplifier, the growth rate of the standing waves in the complete physical process brought about by the bars is equal to the blockage rate of the radiated waves. Via designing a radiation group in Fig. 5c and a corresponding control group in Fig. 5e where the bar does not exist, the blockage rate of the radiated waves (denoted by K_R hereinafter) can be well determined.

In theory, when the harbor suffers from incident monochromatic waves with very small amplitudes, the actual influential degree of the periodic topography on the wave condition inside the harbor should be equal to the product of the attenuation rate of the transmitted waves and the blockage rate of the radiated waves caused by the periodic topography (this equivalence relationship will be proved in subsection 5.3). Hence, the internal coupling mechanism between the periodic topography and the harbor can be effectively revealed by separately studying the transmitted waves' attenuation rate and the radiated waves' blockage rate.

4. Setup of numerical experiments

4.1. Incident wave parameters

In the present study, the effects of the Bragg reflection on long waves inside the harbor under harbor resonance and non-resonance conditions are investigated. Hence, aiming at these two conditions, the parameters for the incident waves are introduced in subsections 4.1.1 and 4.1.2. Only the incident monochromatic waves are adopted for both conditions.

4.1.1. Harbor resonance condition

A long and narrow rectangular harbor with dimensions of 20 m × 2 m is considered. The wa-

ter depth inside is set to a constant, h_0=1 m. According to the theoretical solution of the harbor resonance excited by long linear waves (Mei, 1983), the amplification factor curve of the harbor is shown in Fig. 6. It can be observed that the lowest four resonant modes respectively correspond to the eigenfrequencies of 0.035 Hz, 0.108 Hz, 0.180 Hz, and 0.249 Hz.

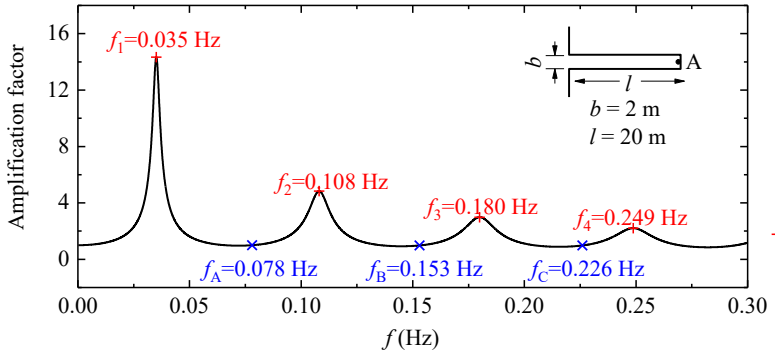

Fig. 6. Amplification factors at the center of the backwall (point A) calculated by Mei's (1983) theoretical solution. f_j (j=1-4) denotes the eigenfrequency of the j^{th} mode (Mode j), and f_j (j= "A" - "C") corresponds to three non-resonant frequencies.

Table 2. Parameters of both the incident waves for Modes 1-4 and the arc-shaped sinusoidal bars for the complete physical process simulations. L_j refers to the wavelength of the incident waves, which is determined by the linear dispersion relation. The topographic parameters in bold are also adopted for the process decomposition simulations.

Mode j	Parameters of incident waves			Parameters of arc-shaped sinusoidal bars		
	f_j (Hz)	L_j/h_0	a/h_0	N	D/h_0	$2S/L_j$
1	0.035	89.41	0.01	0, **2**, **4**, **6**, **8**	0.1, 0.2, 0.3, **0.4**	**0.5-1.5**
2	0.108	28.77	0.01	0, **2**, **4**, **6**, **8**	0.1, 0.2, 0.3, **0.4**	**0.5-1.5**
3	0.180	17.02	0.01	0, **2**, **4**, **6**, **8**	0.1, 0.2, 0.3, **0.4**	**0.5-1.5**
4	0.249	12.05	0.01	0, **2**, **4**, **6**, **8**	0.1, 0.2, 0.3, **0.4**	**0.5-1.5**

To ensure that the lowest four resonant modes can be successfully excited, the frequencies of the incident monochromatic waves are taken to be their separate eigenfrequencies. In all cases, the amplitude of the incident waves is set to a=0.01 m. Specific parameters of the incident waves for the lowest four modes are presented in Table 2, where f_j and L_j (j=1-4) denote the frequency and the wavelength of the incident waves, respectively.

4.1.2. Harbor non-resonance condition

To study the effects of Bragg reflection on the harbor non-resonance condition, incident waves with frequencies of 0.078 Hz, 0.153 Hz, and 0.226 Hz are considered. All their amplification factors are approximately equal to 1.0 (refer to Fig. 6). Hereinafter, these three frequencies are denoted separately by using the variables f_A, f_B, and f_C. All the cases corresponding to the incident waves with f_A, f_B, and f_C are classified into Group A, Group B, and Group C, respectively. The parameters of the incident waves for these three non-resonance groups are listed in Table 3.

Table 3. Parameters of both the incident waves for Groups A-C and the arc-shaped sinusoidal bars for the complete physical process simulations. The topographic parameters in bold are also adopted for the process decomposition simulations. *j* refers to the symbols "A", "B" or "C".

Group *j*	Parameters of incident waves			Parameters of arc-shaped sinusoidal bars		
	f_j (Hz)	L_j/h_0	a/h_0	N	D/h_0	$2S/L_j$
A	0.078	39.99	0.01	0, **8**	**0.4**	**0.5-1.5**
B	0.153	20.15	0.01	0, **8**	**0.4**	**0.5-1.5**
C	0.226	13.38	0.01	0, **8**	**0.4**	**0.5-1.5**

4.2. Numerical wave tank

The NWT for the complete physical process simulations and the coordinate system adopted are illustrated in Fig. 7. As stated above, the harbor has a length of l = 20 m and a width of b = 2 m. Considering that the incident wavelengths vary over a fairly wide range for different resonant modes and different non-resonance groups (see Tables 2 and 3), the dimensions of the computational domain outside the harbor are designed according to the incident wavelength, L_j. Specifically, the length of the domain outside the harbor along the x-axis is set to $8.5L_j$, and hence the total length of the domain along the x-axis is $(8.5L_j+l)$. In the y-axis direction, the entire length of the domain is set to $(16L_j+b)$. The wave-making zone with a width of $0.25L_j$ is deployed to generate the incident waves. The sponge layers with a width of $1.5L_j$ are arranged at the left, upper, and lower boundaries to dissipate reflected/radiated waves.

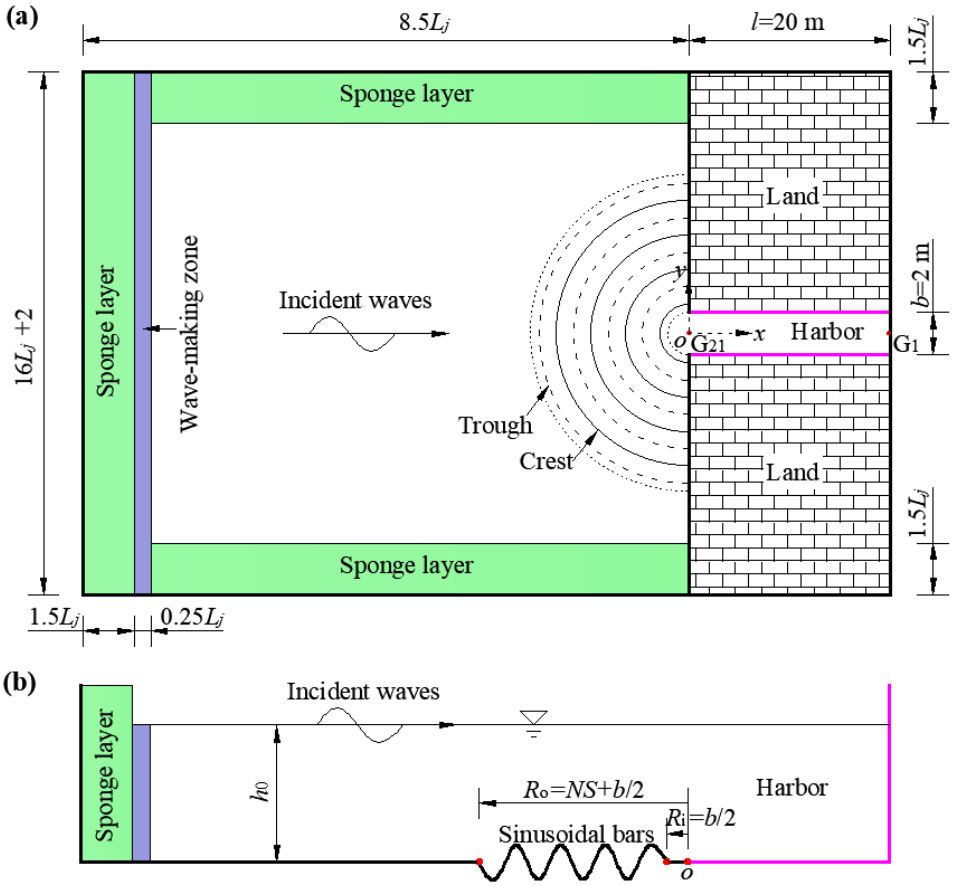

Fig. 7. Sketch of the NWT for the complete physical process simulations and the definition of the coordinate system adopted: (a) the top view of the NWT, (b) the front view of the cross-section with y=0 (taking the sinusoidal bars with N=4 as an example).

For all cases in Modes 2-4 and Groups B and C, the uniform grid sizes of Δx=0.25 m and Δy=0.20 m are adopted in the whole computational domain, where Δx and Δy denote the grid sizes in the x- and the y-axis directions, respectively. While for all cases in Mode 1 and Group A, the uniform grid sizes of Δx=0.25 m and Δy=0.20 m are only utilized inside the harbor. For the grid sizes outside the harbor, they gradually increase from Δx=0.25 m and Δy=0.20 m in the vicinity of the harbor to $\Delta x \approx \Delta y \approx 0.025L_i$ in the sponge layers. The total simulation time is 40 wave periods, and the time step is 0.03 s. To record the wave condition, 21 gauges (i.e., G_1-G_{21}) with an interval of 1 m are arranged inside the harbor and along the centerline of the harbor.

To answer Questions (1), (3), and (4) arisen in the Introduction section, a patch of arc-shaped sinusoidal bars with various geometric parameters is deployed around the harbor entrance, and the crest/trough lines of sinusoidal bars form a series of concentric semicircles centered on the middle

point of the entrance. The geometric parameters of the bars for both the harbor resonance and non-resonance conditions are also listed in Tables 2 and 3, respectively.

For the complete physical process simulations of the harbor resonance condition (i.e., Modes 1-4), four bar amplitudes (i.e., D/h_0=0.1-0.4 in the interval of 0.1) and five bar numbers (i.e., N=0-8 in the interval of 2) are considered; while for that of the non-resonance condition (i.e., Groups A-C), only one bar amplitude (i.e., D/h_0=0.4) and two bar numbers (i.e., N=0 and 8) are studied. It should be emphasized that N=0 implies no bar existing in the computational domain, and the cases with N=0 are simulated here as the comparative group for the instances with N>0. For the physical process decomposition simulations, only the bars with D/h_0=0.4 are considered.

The radius for the inner boundary of the bar patch, R_i, is set to the half-width of the harbor (i.e., b/2=1 m). The dimensionless bar wavelength, $2S/L_j$, varies between 0.5 and 1.5. Hence, the radius for the outer boundary of the bar patch, R_o=NS+1, can achieve a maximum value of ($6L_j$ +b/2) when N=8 and $2S/L_j$=1.5. The water depth inside the whole domain is a constant of h_0=1.0 m except over the bar patch, and thus is formulated as

$$h=\begin{cases} h_0 & \text{when } 0<x<l, |y|\le b/2 \\ h_0-D\sin(2\pi r/S) & \text{when } b/2\le r\le R, x\le 0 \\ h_0 & \text{when } r>R,\ x\le 0 \end{cases}, \tag{10}$$

where r denotes the distance between any spatial point and the middle point of the entrance.

For the process decomposition simulations, the overwhelming majority of the setups for their NWTs are identical to that shown in Fig. 7. Only the different setups between them are described here. For the transmission sub-process and its control group (Fig. 5b and d), the length of the harbor is extended by $1.5L_j$. In this extended domain, a sponge layer is deployed so that all the transmitted waves can be effectively absorbed therein. The attenuation rate of the transmitted waves, K_T, is the ratio of the wave amplitude at the gauge G_1 in the transmission sub-process to that in its control group. For the radiation sub-process and its control group (Fig. 5c and e), the wave-making zone is no longer arranged near the left sponge layer. Instead, it is deployed just outside the harbor entrance. Its width along the y-axis is equal to the width of the harbor, and its width along the x-axis is still set to $0.25L_j$. The blockage rate of the radiated waves, K_R, is the ratio of the wave amplitude at the gauge G_1 in the radiation sub-process to that in its control group.

5. Results and discussion

Time histories of free surface and spatial distributions of wave amplitudes inside the harbor for the complete physical process simulations are first demonstrated in subsection 5.1. Then, the overall influences of Bragg reflection on mitigating the long waves inside the harbor under both the resonance and non-resonance conditions are presented in subsection 5.2. Subsection 5.3 analyzes the internal mitigation mechanism of the long waves based on the physical process decomposition method. Finally, the influences of shape parameters of bars on harbor oscillations are comprehensively studied in subsection 5.4.

5.1. Time histories of wave elevations and amplitude distributions for complete physical processes

5.1.1. Harbor resonance condition

Fig. 8 illustrates the time histories of the wave elevations at the backwall of the harbor (i.e., G_1) for the sinusoidal bars with N=8, D/h_0=0.4, $2S/L_j$=1.0 (j=1-4) and the no-bar topography (i.e., N=0) under Modes 1-4. In this figure, $T_j = 1/f_j$ denotes the incident wave period. The time histories of the wave elevations, η, at the gauge G_1 are normalized by η^*_{max} that denotes the maximum wave elevation during the whole simulation for the no-bar topography. In the initial stage of the simulations, the water body inside the harbor is calm. After around (8-10)T_j, which depends on the resonant modes, the incident waves arrive at the gauge G_1. Then the wave energy increases gradually from zero to its maximum level within around another $10T_j$ for all the eight cases shown in the figure. In other words, at the moment of $t \approx 20T_j$, the steady-state harbor resonance has been obtained. In the current study, only the time histories of the steady-state wave elevations (t/T_j>20) are utilized to analyze the spatial distributions of wave amplitudes inside the harbor.

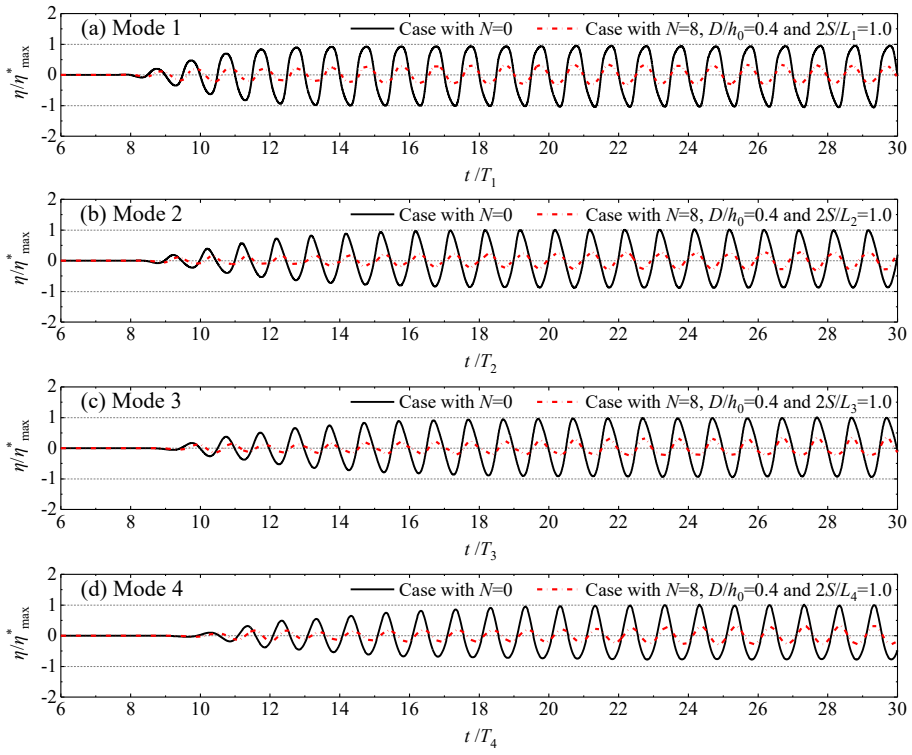

Fig. 8. Time histories of the free surfaces at the gauge G_1 for the sinusoidal bars with N=8, D/h_0=0.4, $2S/L_j$=1.0 (j=1-4) and the no-bar topography (i.e., N=0) under Modes 1-4. T_j=1/f_j in the figure denotes the incident wave period adopted in Mode j.

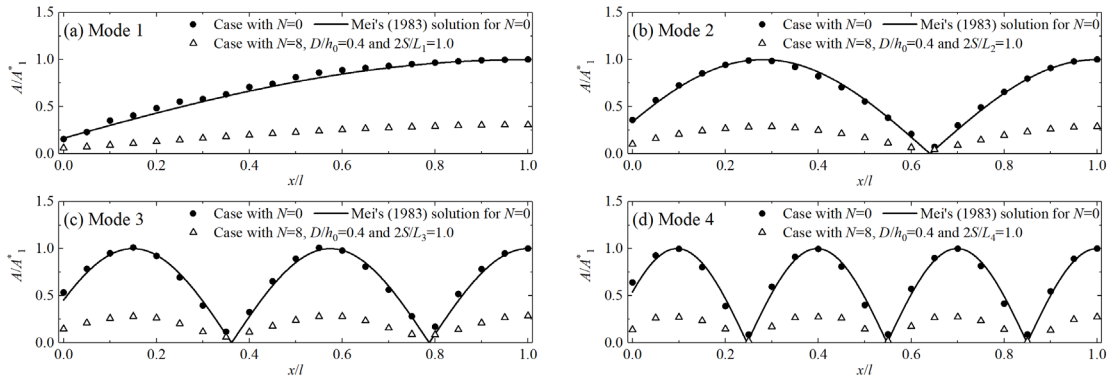

Fig. 9. The amplitude distributions inside the harbor predicted by FUNWAVE 2.0 (dots) and by Mei's (1983) theoretical solution (lines) for the eight cases in Fig. 8.

The mean wave amplitudes at all wave gauges during the t/T_j>20 can be obtained based on the zero-up-crossing method and the time histories of steady-state water elevations. For all the eight cases in Fig. 8, the spatial distributions of the mean wave amplitudes are further demonstrated in Fig. 9, where A denotes the mean wave amplitudes at various gauges, and A^*_1 denotes

the mean wave amplitude at the gauge G_1 for the no-bar topography. The theoretical resonant modal shapes predicted by Mei's (1983) solution are also illustrated here for comparison.

There are three apparent phenomena reflected in this figure. Firstly, a fairly good agreement between the simulated amplitude distributions and the theoretical ones can be observed for all the no-bar cases. It well reflects the accuracy of the FUNWAVE 2.0 model in simulating harbor resonance. Secondly, regardless of whether the bars exist, the maximum wave amplitude always appears at the backwall owing to its total reflection property. Considering the significance and typicality of the wave amplitude at the gauge G_1, the ratio of the amplitude there for N>0 (denoted by A_1) to that for N=0 (denoted by A^*_1) will be utilized to quantitatively measure the influence of the arc-shaped bars on harbor oscillations. Thirdly, the wave amplitudes for the cases with N=8 are always significantly smaller than the corresponding ones for the instances with N=0, regardless of the resonant mode. The amplitude ratios, A_1/A^*_1, for Modes 1-4 are further presented in Table 4. For all four modes, their amplitude ratios are only about 30%, which means that around 70% of the resonant wave amplitude is inhibited by the patch of arc-shaped bars outside the harbor.

Table 4. The ratios of the wave amplitudes at the gauge G_1 for the cases with N=8, D/h_0=0.4, and $2S/L_j$=1.0 (j=1-4) to those for the cases with N=0 under Modes 1-4.

Ratio	Mode 1	Mode 2	Mode 3	Mode 4
A_1/A^*_1 (%)	30.61	28.78	28.54	27.42

5.1.2. Harbor non-resonance condition

Fig. 10 presents the comparisons between the time histories of the wave elevations at the backwall for the bars with N=8, D/h_0=0.3, $2S/L_j$=1.0 (j= "A" - "C") and those for the no-bar topography under Groups A-C. The phenomena shown in this figure are identical to those in Fig. 8, except that the wave energy inside the harbor increases rapidly from zero to its steady state only within (3-4)T_j after the incident waves reach the gauge G_1. However, to maintain consistency with the resonance condition, time histories of wave elevation with t/T_j > 20 are also used for the non-resonance condition to calculate the amplitude distribution inside the harbor.

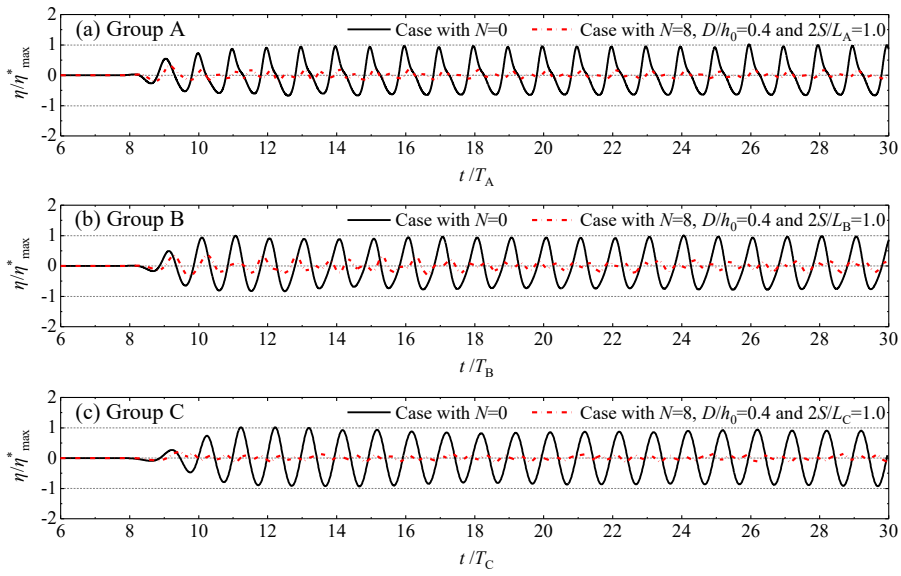

Fig. 10. As in Fig. 8, but for the harbor non-resonance condition. (a)-(c) correspond to Groups A-C, respectively. T_j=1/f_j (j= "A", "B" and "C") denotes the incident wave period utilized in Group j.

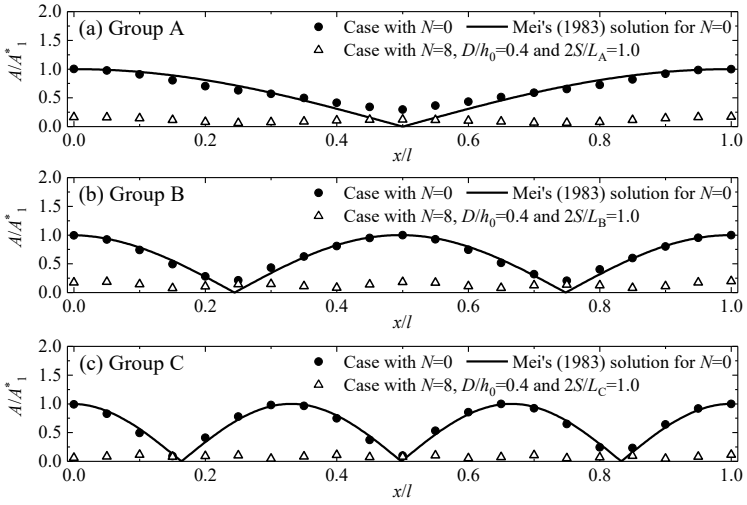

Fig. 11. As in Fig. 9, but for the six cases shown in Fig. 10.

Fig. 11 presents the spatial distributions of the wave amplitudes for all six cases in Fig. 10. Similar to Fig. 9, the following two crucial phenomena are also observed. Firstly, due to the reflective backwall, the maximum wave amplitude inside the harbor always appears there. Secondly, for all three groups, the wave amplitudes for the cases with N=8 are always significantly lower than the corresponding ones for the instances with N=0. Furthermore, the attenuation degree of the wave amplitude caused by the bars for the non-resonance condition seems to be greater than that for the resonance condition. Identical to the resonance condition, the ratio of the amplitude at the

gauge G_1 for N=8 to that for N=0 will also be used to quantitatively determine the influence of the bars on the long waves inside the harbor under the non-resonance condition. The amplitude ratios, A_1/A^*_1, for Groups A-C are further listed in Table 5. It is seen that the amplitude ratios for the three groups are indeed remarkably lower than those for Mode 1-4. For the non-resonance condition, the wave amplitude inside the harbor can be reduced by up to 80% - 89% due to the existence of the bars.

Table 5. The ratios of the amplitudes at the gauge G_1 for the cases with N=8, D/h_0=0.4 and $2S/L_j$=1.0 (j= "A", "B" and "C") to those for the cases with N=0 for Groups A-C.

Ratio	Group A	Group B	Group C
A_1/A^*_1 (%)	16.93	19.61	11.43

5.2. Overall results for the influence of Bragg reflection

The overall results for the effects of the arc-shaped sinusoidal bars on harbor resonance are first shown in subsection 5.2.1, and their ability to restrain harbor resonance is fully revealed. Subsequently, their effects on the long waves inside the harbor under the non-resonance condition are studied in subsections 5.2.2. The similarities and differences of influence characteristics concerning the resonance condition are also uncovered therein.

5.2.1. Harbor resonance condition

Fig. 12 illustrates the changing trends of A_1/A^*_1 with $2S/L_j$ for different bar numbers and resonant modes. There exist three apparent phenomena. Firstly, A_1/A^*_1 seems to be always less than 100% nearby $2S/L_j$=1, and the greater the bar number is, the lower the value of A_1/A^*_1 therein is. Within the ranges of the bar parameters considered, the strength of harbor resonance can be weakened by up to about 80%. It indicates that although the arc-shaped sinusoidal bars can significantly reflect the radiated waves into the harbor when Bragg resonant reflection occurs (refer to Fig. 2), the arc-shaped sinusoidal bars are also able to effectively suppress harbor resonance, just like the periodic bars parallel with the entrance (Gao et al., 2021b). It further implies that besides the possible reason proposed by Gao et al. (2021b) (its detailed description has been presented in

the Introduction section), there exist other unknown mitigation mechanisms of harbor resonance by the periodic topography.

Secondly, in general, the patch of periodic topographies inclines to aggravate harbor resonance as the dimensionless bar wavelength $2S/L_j$ becomes greater than 1.1, especially for Modes 2-4 and for the bars with larger amplitudes. It shows that the intensifying effect of the arc-shaped bars becomes stronger than its inhibitory effect in this case. Thirdly, for each set of the bar number and amplitude, both the lowest A_1/A^*_1 (represented by "$(A_1/A^*_1)_m$" below) and its corresponding $2S/L_j$ (represented by "$(2S/L_j)_m$" and termed as the dimensionless optimal bar wavelength) heavily depend on the geometric parameters of the periodic topography. Specific studies on how the topographic parameters influence them will be implemented in subsections 5.4.

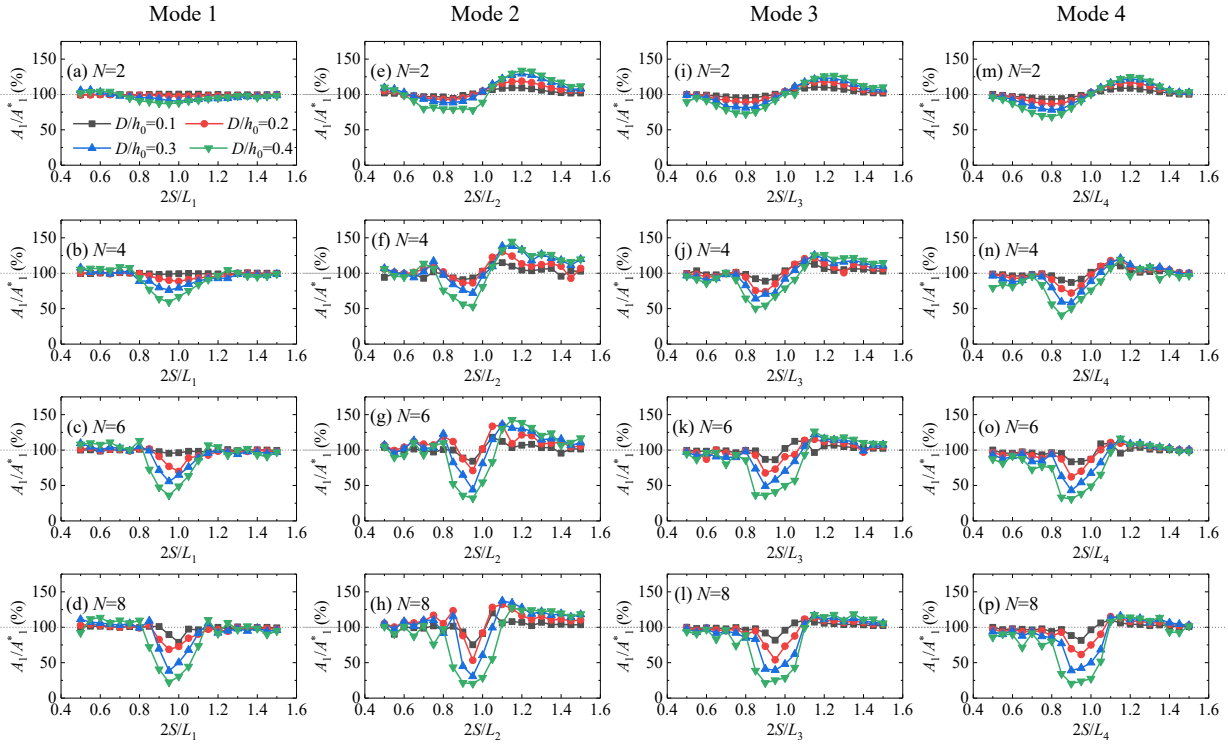

Fig. 12. Changing trends of A_1/A^*_1 with $2S/L_j$ (j=1-4) for different bar numbers: (a-d) Mode 1; (e-h) Mode 2; (i-l) Mode 3; (m-p) Mode 4.

5.2.2. Harbor non-resonance condition

Fig. 13 presents the changing trends of A_1/A^*_1 with $2S/L_j$ for Groups A-C. For comparison, the tendencies of A_1/A^*_1 for Modes 1-3 with N=8 and D/h_0=0.4 are also shown in the figure. It is seen that like the harbor resonance condition, the arc-shaped bars under the non-resonance condi-

tion can also significantly reduce the long waves inside the harbor when the Bragg resonant reflection appears; within the ranges of the bar parameters considered, the strength of the long waves inside the harbor can be weakened by up to about 89%. However, under both conditions, the following three different influence characteristics of the bars exist on the long waves inside the harbor.

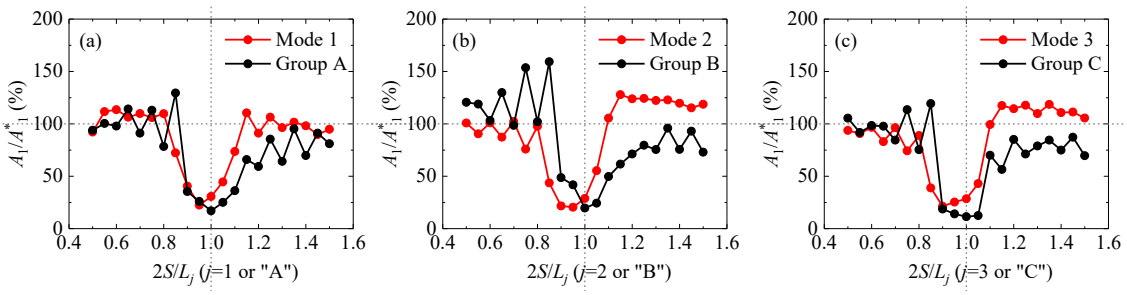

Fig. 13. Changing trends of A_1/A^*_1 with $2S/L_j$ for (a) Group A, (b) Group B, and (c) Group C. For comparison, the tendencies of A_1/A^*_1 for Modes 1-3 with N=8 and D/h_0=0.4 are also shown.

Firstly, within the range of $2S/L_j$ <0.9, the value of A_1/A^*_1 under the non-resonance condition tends to be larger than the corresponding one under the resonance condition. In addition, the former shows a more significant fluctuation. Secondly, their relative size becomes an opposite relationship when $2S/L_j$ becomes larger than 1.0. Furthermore, within this range, the bars always suppress the long waves inside the harbor under the non-resonance condition; on the contrary, under the resonance condition, the bars tend to aggravate the long waves overall. Thirdly, the dimensionless optimal bar wavelengths, $(2S/L_j)_m$, under the non-resonance condition are always equal to or slightly larger than 1.0, while those for the three resonant modes are all less than 1.0.

The internal mitigation mechanism of the long waves inside the harbor by Bragg reflection under both the resonance and non-resonance conditions and the reason for the three different influence characteristics of the topography will be revealed in the following subsection.

5.3. Mechanism analysis of mitigating long waves inside the harbor

Based on the physical process decomposition method, the attenuation rate of the transmitted waves, K_T, and the blockage rate of the radiated waves, K_R, can be quantitatively determined. For the lowest four resonant modes with D/h_0=0.4 and N=8, the values of both K_T and K_R and the

comparison between K_TK_R and A_1/A^*_1 obtained in the complete physical process are illustrated in Fig. 14. Three phenomena can be found. Firstly, the changing trends of K_T with $2S/L_j$ (j=1-4) for the lowest four modes are similar (see Fig. 14a, d, g, and j). Within the ranges of $2S/L_j$>1.2 or $2S/L_j$<0.85, the value of K_T is insensitive to the bar wavelength. The former always slightly fluctuates around a specific value close to 100%. While within the range of $0.85 \leq 2S/L_j \leq 1.2$, K_T continuously decreases and then increases with $2S/L_j$, and all four K_T curves take on a "U" shape. The smallest value of K_T is as low as 13%-18% and always appears at $2S/L_j$=1.0.

Secondly, the changing trends of K_R are distinctly different from those of K_T (see Fig. 14b, e, h, and k). K_R always first decreases, then increases, and then decreases with increasing bar wavelength. In other words, all four K_R curves take on an inverted "N" shape. The maximum value of K_T is 184%-194% and always appears at $2S/L_j$=1.1 or 1.05. Thirdly, for all four resonant modes, the products of K_T and K_R are always very close to the values of A_1/A^*_1 obtained directly in the complete physical process simulations (see Fig. 14c, f, i, and l). It can be quantitatively reflected by the correlation coefficient, R, between the two curves of K_TK_R and A_1/A^*_1. All four correlation coefficients exceed 0.92. This phenomenon proves the correctness of the physical process decomposition method proposed in this paper.

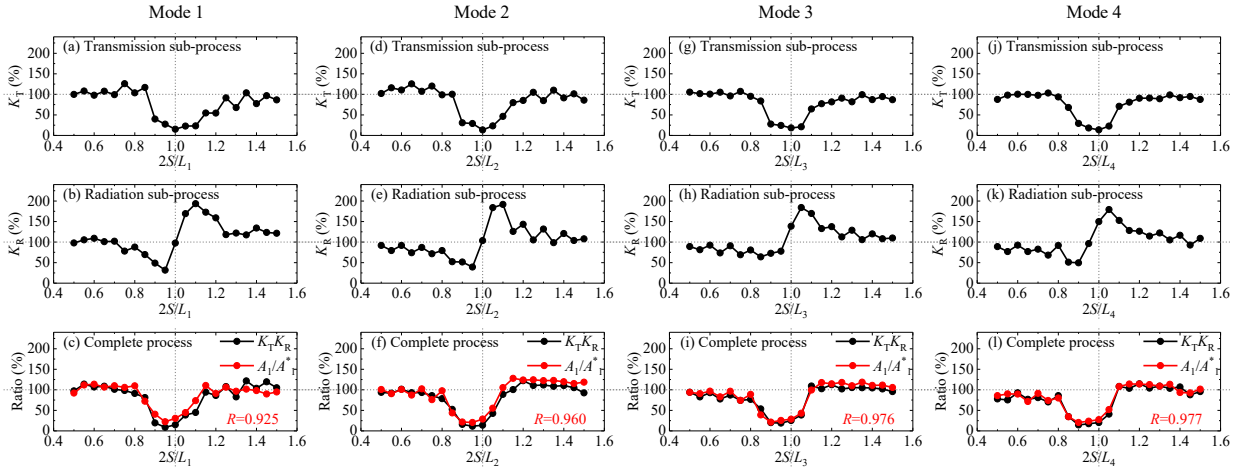

Fig. 14. Attenuation rate of the transmitted waves (K_T), the blockage rate of the radiated waves (K_R), and the comparison of their product with A_1/A^*_1 obtained in the complete physical process simulations with D/h_0=0.4 and N=8: (a-c) Mode 1; (d-f) Mode 2; (g-i) Mode 3; (j-l) Mode 4

To avoid repetition of similar results in this subsection, the results of K_T and K_R and the comparison between K_TK_R and A_1/A^*_1 for the lowest four modes with D/h_0=0.4 and N=2, 4, and 6

are further demonstrated in Figs. A1-A3 of Appendix A. All three phenomena mentioned above are also well observed in Figs. A1-A3.

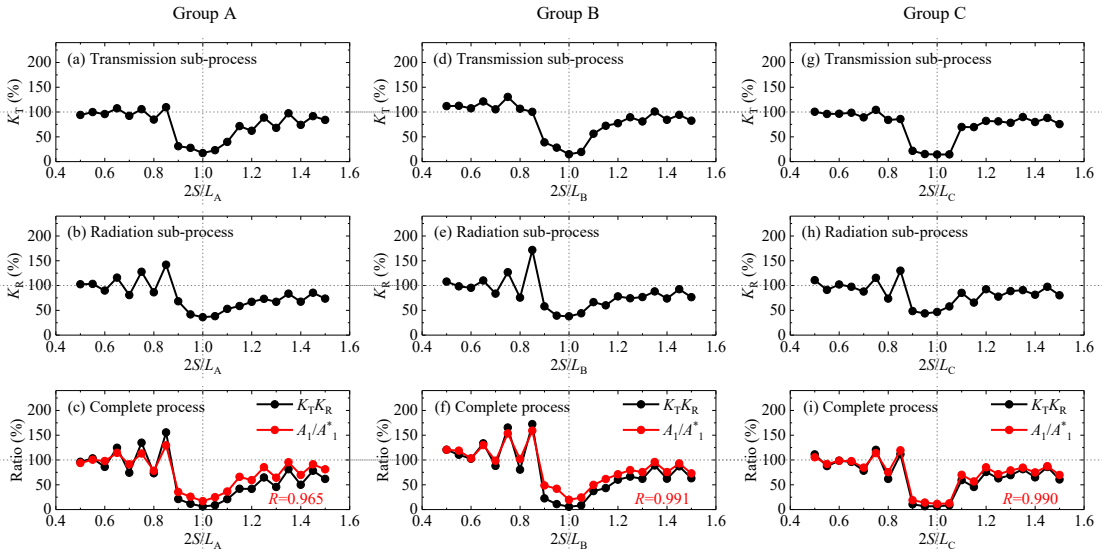

Fig. 15. As in Fig. 14, but for the harbor non-resonance condition: (a-c) Group A; (d-f) Group B; (g-i) Group C.

Fig. 15 further presents the values of K_T and K_R and the comparison between K_TK_R and A_1/A^*_1 for the harbor non-resonance condition. The first and the third phenomena in Fig. 14 are also well observed in this figure. However, for the radiation sub-process (see Fig. 15b, e, and h), the changing trends of K_R are distinctly different from those for Modes 1-4. Specifically, the curve of K_R does not present an inverted "*N*" shape anymore. Instead, within the range of $2S/L_j \leq 0.85$, K_R increases gradually in a fluctuating manner with the increase of $2S/L_j$ (j= "A" - "C"). As the bar wavelength further increases, K_R is always shown to decrease sharply and then mildly increase with the bar wavelength. The maximum value of K_R always appears at $2S/L_j$=0.85 and lies between 130% and 172%, depending on the non-resonance group.

Based on Figs. 14 and 15, it can be concluded that although the possible reason for mitigating harbor resonance by the periodic topography proposed by Gao et al. (2021b) is reasonable, it is not the most critical factor. The essential mechanism lies in that when the Bragg resonant reflection occurs, the enhancement effect of the bars for the long waves inside the harbor caused by the blockage of the radiated waves is much weaker than their attenuation effect caused by the block-

age of the transmitted waves, regardless of the harbor resonance condition or the non-resonance condition.

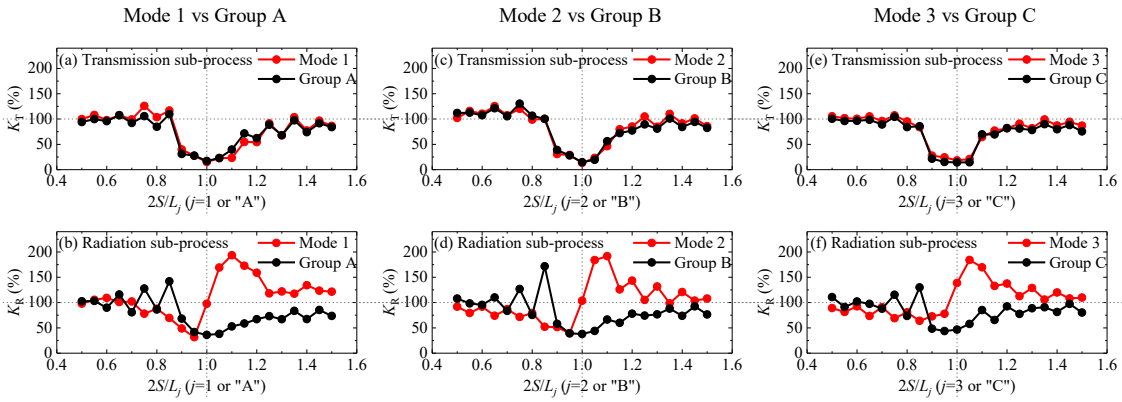

Fig. 16. Comparisons of the changing trends of K_T and K_R with the bar wavelength under the harbor resonance and the non-resonance conditions: (a, b) Mode 1 vs. Group A; (c, d) Mode 2 vs. Group B; (e, f) Mode 3 vs. Group C.

To further reveal the reasons for the three different influence characteristics of the bars on the long waves inside the harbor under the resonance and non-resonance conditions shown in Fig. 13, Fig. 16 intuitively compares the changing trends of both K_T and K_R concerning the bar wavelength under both conditions. It is seen that the two curves of K_T under both conditions are almost overlapped with each other (see Fig. 16a, c, and e). While for K_R under both conditions, as mentioned above, their changing trends are quite different (see Fig. 16b, d, and f). Hence, all the three different influence characteristics of the bars on the long waves inside the harbor are essentially caused by the different influences of the bars on the radiation sub-process.

The first two different influence characteristics can be easily understood from the different changing trends of K_R. The third different influence characteristic needs to be further explained here. For the resonance condition, although the minimum K_T always appears at $2S/L_j$=1.0 or 1.05, the differences between the values of K_T within the range of $0.90 \le 2S/L_j \le 1.05$ are quite small. Hence, the tendencies of $K_T K_R$ (equivalently, A_1/A^*_1) in the vicinity of $2S/L_j$=1.0 depend only on K_R. On the other hand, K_R within the range of $0.80 \le 2S/L_j \le 0.95$ keeps relatively small values. As $2S/L_j$ further increases, the value of K_R increases sharply. Therefore, for Modes 1-4 with N=8 and D/h_0=0.4, their optimal bar wavelengths, $(2S/L_j)_m$, are always less than 1.0. For the non-resonance

condition, the variation of K_R in the vicinity of $2S/L_j$=1.0 is very similar to that of K_T. That is, the minimum K_R always occurs at around $2S/L_j$=1.0, and the variation of K_R within $0.90 \leq 2S/L_j \leq 1.05$ is also quite limited. Because K_T is much smaller than the corresponding K_R within this range, the sensitivity for the variation of A_1/A^*_1 would be controlled mainly by K_T. Hence, for Groups A-C, their optimal bar wavelengths, $(2S/L_j)_m$, are always equal to or slightly larger than 1.0.

5.4. Influences of topographic parameters on harbor oscillations

5.4.1. Influences of the bar number

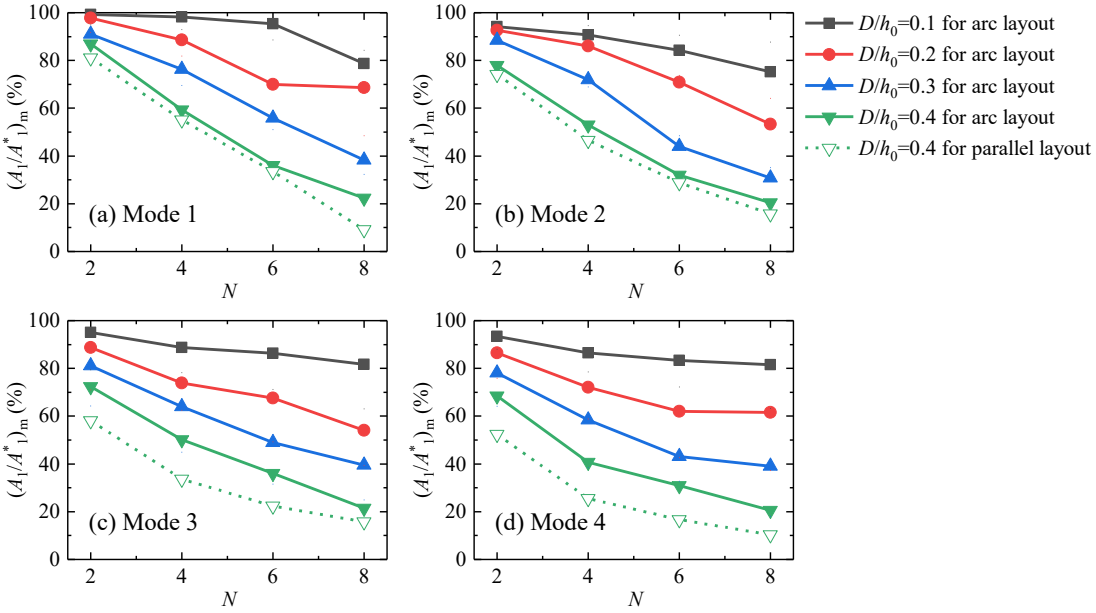

Fig. 17. Changing trends of $(A_1/A^*_1)_m$ with the bar number N for Modes 1-4. Its changing trends for the parallel bars with D/h_0=0.4 in Gao et al. (2021b) are also shown for comparison.

As mentioned above, for each set of the bar number and amplitude, $(A_1/A^*_1)_m$ denotes the minimum value of A_1/A^*_1 within the variation range of the normalized bar wavelength (i.e., $0.5 \leq 2S/L_j \leq 1.5$). Hence, the magnitudes of $(A_1/A^*_1)_m$ can directly reflect the alleviation/inhibition effect of the periodic undulating topography on harbor resonance; the smaller the value of $(A_1/A^*_1)_m$ is, the better the inhibition effect on harbor resonance is. The changing trends of $(A_1/A^*_1)_m$ with the bar number for the lowest four modes are presented in Fig. 17. For ease of comparing the differences between the parallel and arc-shaped bars in inhibiting harbor resonance,

the values of $(A_1/A^*_1)_m$ for the parallel bars with D/h_0=0.4 in Gao et al. (2021b) are also shown in this figure. This comparison is appropriate because the harbors adopted in both studies have identical plane sizes and water depths. In addition, the water depth outside the harbor in these two studies is also the same, except over the patch of bars owing to their different plane layouts.

It can be observed that for all the modes and all bar amplitudes considered, $(A_1/A^*_1)_m$ gradually declines as the bar number rises. It means that when Bragg resonant reflection occurs, the inhibition effect of the arc-shaped periodic topography on harbor resonance becomes better and better as the bar number grows. This phenomenon is consistent with the finding in many pure Bragg reflection investigations (e.g., Gong et al. (2022); Liu et al. (2019); Ni and Teng (2021b)) that the peak Bragg reflection increases gradually with the bar number. It is also seen that the inhibition effect for the arc-shaped bars is always slightly weaker than that for the parallel ones. This phenomenon directly proves that the possible mechanism proposed by Gao et al. (2021b) (shown in Fig. 1) is also reasonable, although it is not the most important and essential factor.

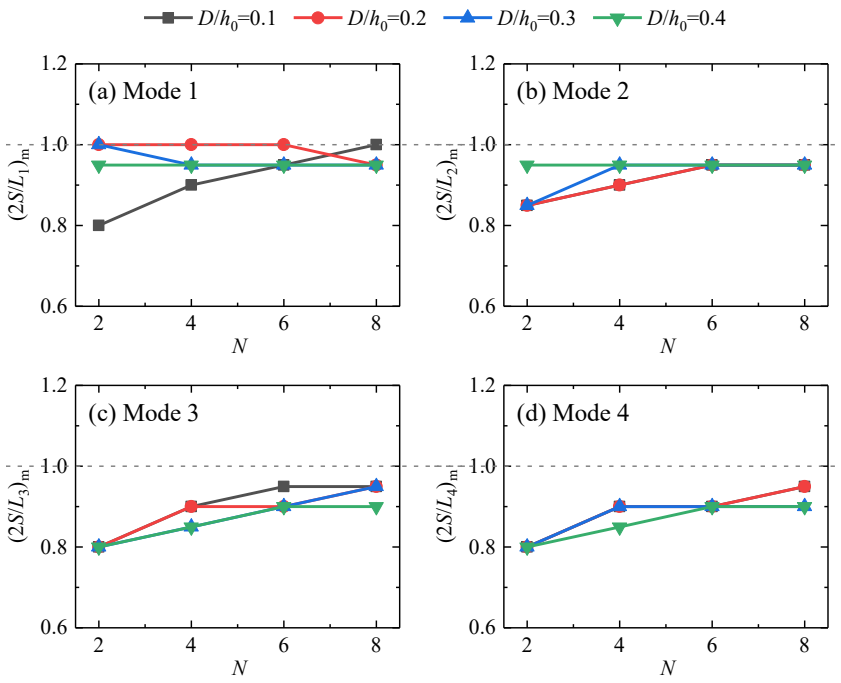

Fig. 18. Changing trends of $(2S/L_j)_m$ with the bar number N for Modes 1-4.

Considering that the dimensionless optimal bar wavelength, $(2S/L_j)_m$, directly reflects the geometric conditions attaining the best inhibition effect, an accurate understanding of it is also

important. The changing trends of $(2S/L_j)_m$ with the bar number for the lowest four modes are shown in Fig. 18. Two apparent phenomena can be observed. Firstly, for most sets of the bar number and the bar amplitude, their values of $(2S/L_j)_m$ are less than 1.0. This phenomenon is mainly determined by the changing feature of K_R, which has been explained in detail in subsection 5.3. Secondly, except for the bars with D/h_0=0.2-0.4 in Mode 1 and the bars with D/h_0=0.4 in Mode 2, the values of $(2S/L_j)_m$ for the other bars increase gradually with the bar number.

5.4.2. Influences of the bar amplitude

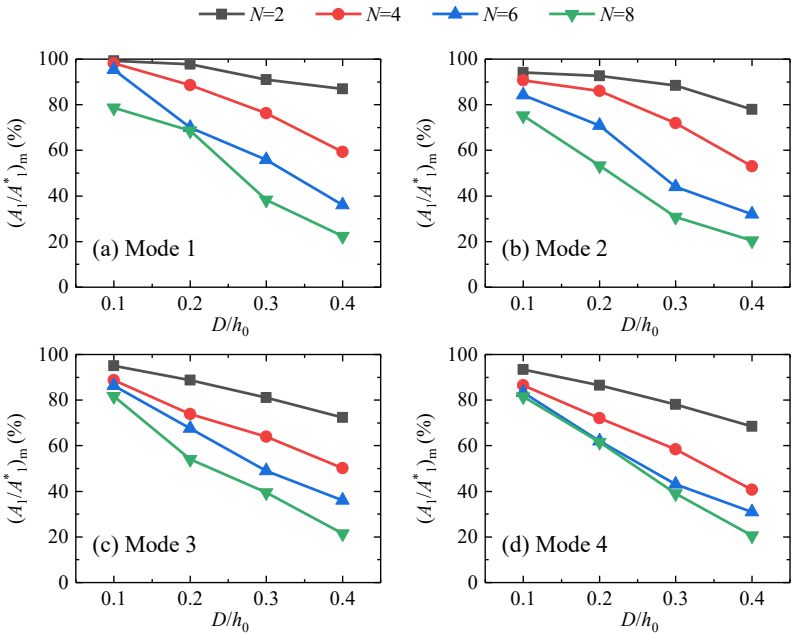

Fig. 19. Variations of $(A_1/A^*_1)_m$ with the bar amplitude for Modes 1-4.

The variation of $(A_1/A^*_1)_m$ with the bar amplitude for each mode and each bar number is illustrated in Fig. 19. Similar to Fig. 17, for all the modes and all the bar numbers considered, $(A_1/A^*_1)_m$ also decreases gradually with an increase of the bar amplitude, which indicates that the inhibition effect of the arc-shaped bars on harbor resonance is progressively enhanced as the bar amplitude rises. Fig. 20 further shows the tendency of $(2S/L_j)_m$ concerning the bar amplitude. The influence of the bar amplitude on $(2S/L_j)_m$ is shown to rely heavily on the resonant mode. Specifically, for Mode 1, as the bar amplitude increases, $(2S/L_j)_m$ may slightly decrease or first increase and then decrease with the former, depending on the bar number. For Mode 2, $(2S/L_j)_m$ keeps un-

changed or increases slightly with the rise of the bar amplitude. While for Modes 3 and 4, the increase of the bar amplitude tends to cause the decline of $(2S/L_j)_m$.

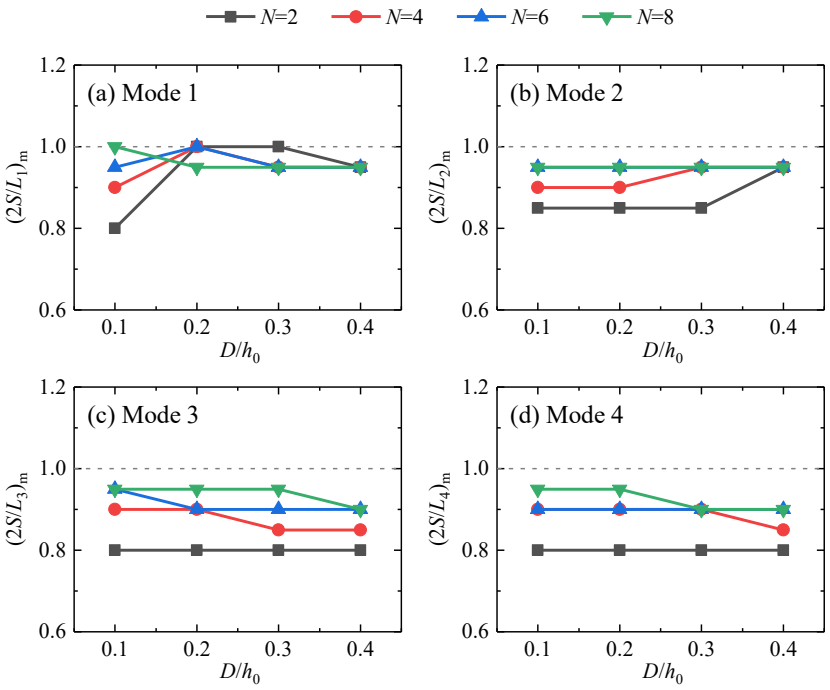

Fig. 20. Variations of $(2S/L_i)_m$ with the bar amplitude for Modes 1-4.

6. Conclusions

In the present study, the interactions between a patch of arc-shaped sinusoidal bars and the harbor subjected to the incident monochromatic long waves are investigated for the first time by adopting the FUNWAVE 2.0 model. The influences of the arc-shaped bars on two types of wave conditions inside the harbor (i.e., the harbor resonance condition and the non-resonance one) are systematically studied. For the harbor resonance condition, the lowest four resonant modes (i.e., Modes 1-4) are considered; for the non-resonance one, three non-resonant groups (i.e., Groups A-C) are designed. To reveal the coupling mechanism between the bars and the harbor, an ingenious physical process decomposition method that separates the complete physical process into a transmission sub-process and a radiation one is proposed. The present study confirms its correctness. Based on this analysis method, the internal influence mechanism of Bragg reflection on the long waves inside the harbor is revealed first. Then, the similarities and differences of the influence characteristics of Bragg reflection under the harbor resonance and non-resonance conditions

are also uncovered and explained. Finally, for the harbor resonance condition, the influences of the two topographic parameters (i.e., the bar number and the bar amplitude) on the best mitigation/inhibition effect and on the optimal bar wavelength that can attain the best inhibition effect are discussed. The results of this article have expanded our understanding on harbor resonance and provide a solid theoretical basis for possible practical engineering applications in the future.

The following conclusions are drawn from the present study:

1. For both the harbor resonance and non-resonance conditions, the capability of the patch of arc-shaped sinusoidal bars to effectively inhibit the long waves inside the harbor is proved. Within the ranges of the bar parameters considered, the amplitude of the long waves inside the harbor can be weakened by up to about 80% and 89%, respectively, for the two conditions. The confirmation of the capability, as mentioned above, implies that the possible mechanism proposed by Gao et al. (2021b) (shown in Fig. 1) is not the most critical factor for the periodic topography to mitigate the long waves inside the harbor significantly.
2. Based on the physical process decomposition method proposed, the most critical and essential mechanism for the periodic topography to mitigate the long waves inside the harbor is revealed for the first time. That is, when the Bragg resonant reflection occurs, the enhancement effect of the periodic topography on the long waves inside the harbor caused by the blockage of the radiated waves is much weaker than its attenuation effect caused by the blockage of the transmitted waves, regardless of the harbor resonance condition or the non-resonance condition.
3. Three different influence characteristics of the bars exist on the long waves inside the harbor under resonance and non-resonance conditions. (1) A_1/A^*_1 at $2S/L_j$ <0.9 under the non-resonance condition tends to be greater than the corresponding one for the resonance condition. (2) When $2S/L_j > 1.0$, the bars under the non-resonance condition always suppress the long waves inside the harbor, while the bars under the resonance condition tend to aggravate the latter overall. (3) The dimensionless optimal bar wavelengths denoted by $(2S/L_j)_m$ under the non-resonance condition are always equal to or slightly larger than 1.0, while those for the resonance condition are less than 1.0. The differences in all these three aspects are essentially caused by the different influence characteristics of the bars on the radiation sub-process under both conditions.

4. For the harbor resonance condition, the best inhibition effect of Bragg reflection over the arc-shaped bars on the long waves inside the harbor is gradually strengthened as the amplitude or the number of bars increases. In general, the optimal bar wavelength, $(2S/L_j)_m$, is shown to increase gradually with the bar number, especially for Modes 2-4. However, the influence features of the bar amplitude on $(2S/L_j)_m$ heavily rely on the resonant mode.
5. Via directly comparing the differences between the values of $(A_1/A^*_1)_m$ for the arc-shaped bars and those for the parallel bars with the same amplitude, it is found that for the cases considered where the incident angle of the waves is normal to the harbor entrance, the mitigation effect on harbor resonance for the arc-shaped bars is always slightly weaker than that for the parallel ones. This phenomenon directly proves that the possible mechanism proposed by Gao et al. (2021b) is also reasonable, although it is not the most important and essential factor.

Finally, we affirm that these conclusions are only valid for the given harbor, monochromatic incident waves, arc-shaped sinusoidal bars, and the parameter variation ranges for both the incident waves and the bars considered in the present study.

Acknowledgments

This research is financially supported by the Open Research Fund of Key Laboratory of Water Security Guarantee in Guangdong-Hong Kong-Marco Greater Bay Area of Ministry of Water Resources (Grant No. WSGBA-KJ202309), the Guangdong Basic and Applied Basic Research Foundation (Grant No. 2023A1515010890), the Science and Technology Development Fund, Macau SAR (Project No. 0009/2021/A, SKL-IOTSC(UM)-2021-2023), and the Royal Society (Grant No. IEC\NSFC\181321).

References

Alam, M.-R., Liu, Y., Yue, D.K.P., 2010. Oblique sub- and super-harmonic Bragg resonance of surface waves by bottom ripples. Journal of Fluid Mechanics 643, 437-447.

Araújo, R., Alfredini, P., Amaral, R.F.D., 2004. Sand waves of the navigation channel of the Ponta da Madeira Harbour (Brazil). Proceedings of the 29th Conference on Coastal Engineering, Lisbon, Portugal, pp. 2558-2567.

Bruno, D., Serio, F.D., Mossa, M., 2009. The FUNWAVE model application and its validation

using laboratory data. Coastal Engineering 56 (7), 773-787.

Chawla, A., Kirby, J.T., 2000. A source function method for generation of waves on currents in Boussinesq models Applied Ocean Research 22 (2), 75-83.

Chen, M.-Y., Mei, C.C., Chang, C.-K., 2006. Low-frequency spectra in a harbour excited by short and random incident waves. Journal of Fluid Mechanics 563, 261-281.

Davies, A.G., 1982. On the interaction between surface waves and undulations on the seabed. Journal of Marine Research 40 (2), 331-368.

De Jong, M.P.C., Battjes, J.A., 2004. Seiche characteristics of Rotterdam Harbour. Coastal Engineering 51 (5-6), 373-386.

Dodd, N., Blondeaux, P., Calvete, D., Swart, H.E.D., Falqués, A., Hulscher, S.J.M.H., Różyński, G., Vittori, G., 2003. Understanding coastal morphodynamics using stability methods. Journal of Coastal Research 19 (4), 849-865.

Dong, G., Wang, G., Ma, X., Ma, Y., 2010a. Harbor resonance induced by subaerial landslide-generated impact waves. Ocean Engineering 37 (10), 927-934.

Dong, G., Wang, G., Ma, X., Ma, Y., 2010b. Numerical study of transient nonlinear harbor resonance. Science China-Technological Sciences 53, 558-565.

Dong, G., Zheng, Z., Gao, J., Ma, X., Dong, Y., Wu, H., 2020. Experimental investigation on special modes with narrow amplification diagrams in harbor oscillations. Coastal Engineering 159, 103720.

Dong, Y., Ma, Y., Ma, X., Zheng, Z., Dong, G., 2022. Topographic influence on special modes with narrow amplification diagrams in harbor oscillations. Ocean Engineering 258, 111687.

Dong, Y., Zheng, Z., Ma, Y., Gao, J., Ma, X., Dong, G., 2023. Numerical investigation on the mitigation of harbor oscillations by periodic undulating topography. Ocean Engineering 279, 114580.

Fabrikant, A.L., 1995. Harbor oscillations generated by shear flow. Journal of Fluid Mechanics 282, 203-217.

Fan, J., Zheng, J., Tao, A., Liu, Y., 2021. Upstream-propagating waves induced by steady current over a rippled bottom: theory and experimental observation. Journal of Fluid Mechanics 910, A49. doi:10.1017/jfm.2020.1006.

Gao, J., Bi, W., Zhang, J., Zang, J., 2023. Numerical investigations on harbor oscillations induced by falling objects. China Ocean Engineering. https://doi.org/10.1007/s13344-023-0038-y.

Gao, J., Ji, C., Gaidai, O., Liu, Y., 2016. Numerical study of infragravity waves amplification during harbor resonance. Ocean Engineering 116, 90-100.

Gao, J., Ji, C., Gaidai, O., Liu, Y., Ma, X., 2017. Numerical investigation of transient harbor oscillations induced by N-waves. Coastal Engineering 125, 119-131.

Gao, J., Ma, X., Chen, H., Zang, J., Dong, G., 2021a. On hydrodynamic characteristics of transient harbor resonance excited by double solitary waves. Ocean Engineering 219, 108345.

Gao, J., Ma, X., Dong, G., Chen, H., Liu, Q., Zang, J., 2021b. Investigation on the effects of Bragg reflection on harbor oscillations. Coastal Engineering 170, 103977.

Gao, J., Ma, X., Zang, J., Dong, G., Ma, X., Zhu, Y., Zhou, L., 2020. Numerical investigation of harbor oscillations induced by focused transient wave groups. Coastal Engineering 158, 103670.

Gao, J., Zhou, X., Zang, J., Chen, Q., Zhou, L., 2018a. Influence of offshore fringing reefs on infragravity period oscillations within a harbor. Ocean Engineering 158, 286-298.

Gao, J., Zhou, X., Zhou, L., Zang, J., Chen, H., 2019. Numerical investigation on effects of fringing reefs on low-frequency oscillations within a harbor. Ocean Engineering 172, 86-95.

Gao, J., Zhou, X., Zhou, L., Zang, J., Chen, Q., Ding, H., 2018b. Numerical study of harbor oscillations induced by water surface disturbances within harbors of constant depth. Ocean Dynamics 68 (12), 1663–1681.

Goda, Y., Suzuki, T., 1976. Estimation of incident and reflected waves in random wave experiments, Proceedings of the 15th Coastal Engineering Conference, Honolulu, Hawaii, pp. 828-845.

Gong, Q., Jiang, M.-T., Pang, C.-L., Zhang, X.-J., Chen, X.-Y., Ni, Y.-L., 2022. Wave energy reflection by the Bragg breakwater composed of rectangular bars on the horizontal permeable seabed. Energy Reports 8, 566-573.

Gonzalez-Escriva, J.A., Medina, J.R., Garrido, J.M., 2020. Port resonance mitigation modeled introducing ARJ-R structures, Proceedings of the 36th Virtual International Conference on Coastal Engineering.

Gulshan, Kumar, P., Rajni, 2020. Moored ship motion analysis in Paradip port under the resonance conditions using 3-D boundary element method. Journal of Marine Science and Technology 25, 1075-1092.

Guo, F.-C., Liu, H.-W., Pan, J.-J., 2021. Phase downshift or upshift of Bragg resonance for water wave reflection by an array of cycloidal bars or trenches. Wave Motion 106, 102794.

Hao, J., Li, J., Liu, S., Wang, L., 2022. Wave amplification caused by Bragg resonance on parabolic-type topography. Ocean Engineering 244 110442.

Isaacson, M., Qu, S., 1990. Waves in a harbour with partially reflecting boundaries. Coastal Engineering 14 (3), 193-214.

Kar, P., Koley, S., Sahoo, T., 2020. Bragg scattering of long waves by an array of trenches. Ocean Engineering 198, 107004.

Kaur, S., Kumar, P., Rajni, 2022. Non-linear periodic long waves based on Boussinesq equation for shallow water waves: A coupled FEM modeling. Ocean Engineering 245, 110469.

Kirby, J.T., Long, W., Shi, F., 2003. Funwave 2.0 Fully Nonlinear Boussinesq Wave Model On Curvilinear Coordinates. Report No. CACR-02-xx. Center for Applied Coastal Research, Dept. of Civil & Environmental Engineering, University of Delaware, Newark, Delaware.

Knapp, R.T., Vanoni, V.A., 1945. Wave and surge study for the Naval Operating Base, Terminal Island, Callfornia. California Institute of Technology, Pasadena, CA.

Kulikov, E.A., Rabinovich, A.B., Thomson, R.E., Bornhold, B.D., 1996. The landslide tsunami of November 3, 1994, Skagway Harbor, Alaska. Journal of Geophysical Research 101 (3), 6609-6615.

Kumar, P., Zhang, H., Kim, K.I., Yuen, D.A., 2016. Modeling wave and spectral characteristics of moored ship motion in Pohang New Harbor under the resonance conditions. Ocean Engineering 119, 101-113.

Lee, J.J., 1971. Wave induced oscillations in harbours of arbitrary geometry. Journal of Fluid Mechanics 45, 375-394.

Lee, J.J., Xing, X., 2009. Computer modeling for harbor planning and design, in: Kim, Y.C. (Ed.), Handbook of Coastal and Ocean Engineering. World Scientific Publishing, Singapore, pp. 695-722.

Leys, V., Fernandez, V., Kolijn, D., 2018. Resonant oscillations in small craft harbours:

observations and mitigation modeling examples from Atlantic Canada, Proceedings of the 36th International Conference on Coastal Engineering, Baltimore, Maryland.

Liu, H.-W., 2023. An approximate law of Class I Bragg resonance of linear shallow-water waves excited by five types of artificial bars. Ocean Engineering 267, 113245.

Liu, H.-W., Guo, F.-C., Ni, Y.-L., 2022a. Analytical modeling of the wave reflection by a single cycloidal geotube or trench based on the modified mild-slope equation. Journal of Engineering Mechanics 148 (2), 04021152.

Liu, H.-W., Li, X.-F., Lin, P., 2019. Analytical study of Bragg resonance by singly periodic sinusoidal ripples based on the modified mild-slope equation. Coastal Engineering 150, 121–134.

Liu, P.L.-F., 1986. Effects of depth discontinuity on harbor oscillations. Coastal Engineering 10, 395-404.

Liu, W., Liu, Y., Zhao, X., Ning, Y., 2022b. Numerical study of irregular wave propagation over sinusoidal bars on the reef flat. Applied Ocean Research 121, 103114.

Liu, Y., Zheng, S., Liang, H., Cong, P., 2022c. Wave interaction and energy absorption from arrays of complex-shaped point absorbers. Physics of Fluids 34, 097107.

Ma, X., Zheng, Z., Gao, J., Wu, H., Dong, Y., Dong, G., 2021. Experimental investigation of transient harbor resonance induced by solitary waves. Ocean Engineering 230, 109044.

Ma, X., Zheng, Z., Zhang, X., Dong, G., 2020. Numerical investigation on special modes with narrow amplification diagram in harbor oscillations. Ocean Dynamics 70, 1-19.

Maa, J.P.-Y., Tsai, C.-H., Juang, W.-J., Tseng, H.-M., 2011. A preliminary study on Typhoon Tim induced resonance at Hualien Harbor, Taiwan. Ocean Dynamics 61, 411-423.

Mahmoudof, S.M., Azizpour, J., Eyhavand-Koohzadi, A., 2021. Observation of infragravity wave processes near the coastal cliffs of Chabahar (Gulf of Oman). Estuarine, Coastal and Shelf Science 251, 107226.

Mahmoudof, S.M., Siadatmousavi, S.M., 2020. Bound infragravity wave observations at the Nowshahr beaches, southern Caspian Sea. Applied Ocean Research 98, 102122.

Malej, M., Shi, F., Smith, J.M., Cuomo, G., Tozer, N., 2021. Boussinesq-type modeling of low-frequency wave motions at Marina di Carrara. Journal of Waterway, Port, Coastal and Ocean Engineering 147 (6), 05021015.

Maravelakis, N., Kalligeris, N., Lynett, P.J., Skanavis, V.L., Synolakis, C.E., 2021. Wave overtopping due to harbour resonance. Coastal Engineering 169, 103973.

Mei, C.C., 1983. The Applied Dynamics of Ocean Surface Waves. Wiley, New York.

Mei, C.C., Agnon, Y., 1989. Long-period oscillations in a harbour induced by incident short waves. Journal of Fluid Mechanics 208, 595-608.

Mei, C.C., Hara, T., Naciri, M., 1988. Note on Bragg scattering of water waves by parallel bars on the seabed. Journal of Fluid Mechanics 186, 147 - 162.

Miles, J.W., 1974. Harbor seiching. Annual Review of Fluid Mechanics 6, 17-33.

Ni, Y.-L., Teng, B., 2021a. Bragg resonant reflection of water waves by a Bragg breakwater with porous rectangular bars on a sloping permeable seabed. Ocean Engineering 235, 109333.

Ni, Y.-L., Teng, B., 2021b. Bragg resonant reflection of water waves by a Bragg breakwater with porous trapezoidal bars on a sloping permeable seabed. Applied Ocean Research 114, 102770.

Ning, D.Z., Zhang, S.B., Chen, L.F., Liu, H.W., Teng, B., 2022. Nonlinear Bragg scattering of surface waves over a two-dimensional periodic structure. Journal of Fluid Mechanics 946, A25.

Pan, Y., Yin, S., Chen, Y.P., Yang, Y.B., Xu, C.Y., Xu, Z.S., 2022. An experimental study on the evolution of a submerged berm under the effects of regular waves in low-energy conditions. Coastal Engineering 176, 104169.

Peng, J., Tao., A.F., Fan, J., Zheng, J.H., Liu, Y.M., 2022. On the downshift of wave frequency for Bragg resonance. China Ocean Engineering 36 (1), 76–85.

Priya, P., Kumar, P., Rajni, 2023. Mathematical modelling of nonlinear pressure drops in arbitrarily shaped port utilizing dual boundary element method. Ocean Engineering 275, 114154.

Rabinovich, A.B., 2009. Seiches and harbor oscillations, in: Kim, Y. (Ed.), Handbook of Coastal and Ocean Engineering. World Scientific Publishing, Singapore, pp. 193-236.

Rupali, Kumar, P., Rajni, 2020. Spectral wave modeling of tsunami waves in Pohang New Harbor (South Korea) and Paradip Port (India). Ocean Dynamics 70, 1515-1530.

Russell, K.S., 1982. Coastal Engineering in South Africa, Proceedings of the 18th International Conference on Coastal Engineering, Cape Town, South Africa.

Sakakibara, S., Kubo, M., 2008. Characteristics of low-frequency motions of ships moored inside ports and harbors on the basis of field observations. Marine Structures 21, 196-223.

Sammartino, S., Garrido, J.C.S., Delgado, J., Naranjo, C., Aldeanueva, F.C., Lafuente, J.G., 2014. Experimental and numerical characterization of harbor oscillations in the port of Málaga, Spain. Ocean Engineering 88, 110-119.

Shao, D., Zheng, J., Wang, G., Chen, S., Jiang, G., 2023. Effects of the reef roughness on the harbor oscillations induced by low-frequency waves. Ocean Engineering 273, 113967.

Sun, Q., Niu, X., 2021. Harbor oscillation induced by atmospheric pressure disturbances moving in different directions. Coastal Engineering Journal 64 (2), 217-228.

Wang, G., Zheng, J., Liang, Q., Zhang, W., Huang, C., 2015. Theoretical analysis of harbor resonance in harbor with an exponential bottom profile. China Ocean Engineering 29 (6), 821-834.

Wang, G., Zheng, J., Liang, Q., Zheng, Y., 2014. Analytical solutions for oscillations in a harbor with a hyperbolic-cosine squared bottom. Ocean Engineering 83, 16-23.

Wei, G., Kirby, J.T., Grilli, S.T., Subramanya, R., 1995. A fully nonlinear Boussinesq model for surface waves. Part 1. Highly nonlinear unsteady waves. Journal of Fluid Mechanics 294, 71-92.

Xie, J.-J., 2022. Long wave reflection by an array of submerged trapezoidal breakwaters on a sloping seabed. Ocean Engineering 252, 111138.

Xie, J.-J., Liu, H.-W., 2023. Analytical study of Bragg resonances by a finite periodic array of congruent trapezoidal bars or trenches on a sloping seabed. Applied Mathematical Modelling 119, 717-735.

Xu, J., Chen, L., Ning, D., Zhao, M., 2023. Resonance of water waves propagating over a uniform and a graded line array of rectified submerged cosinoidal bars. Applied Ocean Research 134, 103531.

Yu, X., Chwang, A.T., 1994. Wave-induced oscillation in harbor with porous breakwaters. Journal of Waterway, Port, Coastal, and Ocean Engineering 120 (2), 125-144.

Zhao, H., Yang, J., Chen, G., 2014. Tieshan Port Development Plan: Evaluation of the Long Wave Induced Resonance Using a Numerical Mild-Slope Model. Applied Mechanics and Materials 580-583, 2154-2165.

Zhao, X., Li, Y., Zou, Q., Han, D., Geng, J., 2022. Long waves absorption by a dual purpose Helmholtz-resonance OWC breakwater. Coastal Engineering, 104203.

Zheng, Z., Ma, X., Ma, Y., Perlin, M., Dong, G., 2021. Numerical investigation of seismic-induced harbor oscillations. Coastal Engineering 165, 103838.

Zheng, Z., Ma, X., Yan, M., Ma, Y., Dong, G., 2022. Hydrodynamic response of moored ships to seismic-induced harbor oscillations. Coastal Engineering 176, 104147.

Appendix A: Supplement to subsection 5.3

In subsection 5.3, only the values of both K_T and K_R and the comparison between K_TK_R and A_1/A^*_1 for the lowest four resonant modes with D/h_0=0.4 and N=8 are presented. In fact, as shown in Table 2, the process decomposition simulations are also performed for the lowest four resonant modes with D/h_0=0.4 and N=2, 4 and 6. Here, as the supplement to subsection 5.3, the results of both K_T and K_R and the comparisons between K_TK_R and A_1/A^*_1 for the periodic bars with D/h_0=0.4 and N=2, 4 and 6 are demonstrated in Fig. A1-A3, respectively.

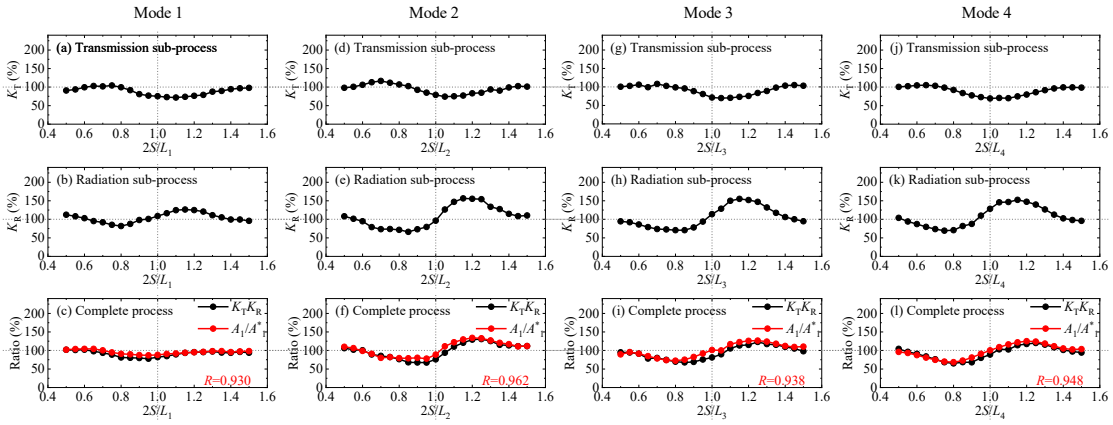

Fig. A1. Values of K_T, K_R and the comparison of their product with A_1/A^*_1 with D/h_0=0.4 and N=2: (a-c) Mode 1; (d-f) Mode 2; (g-i) Mode 3; (j-l) Mode 4

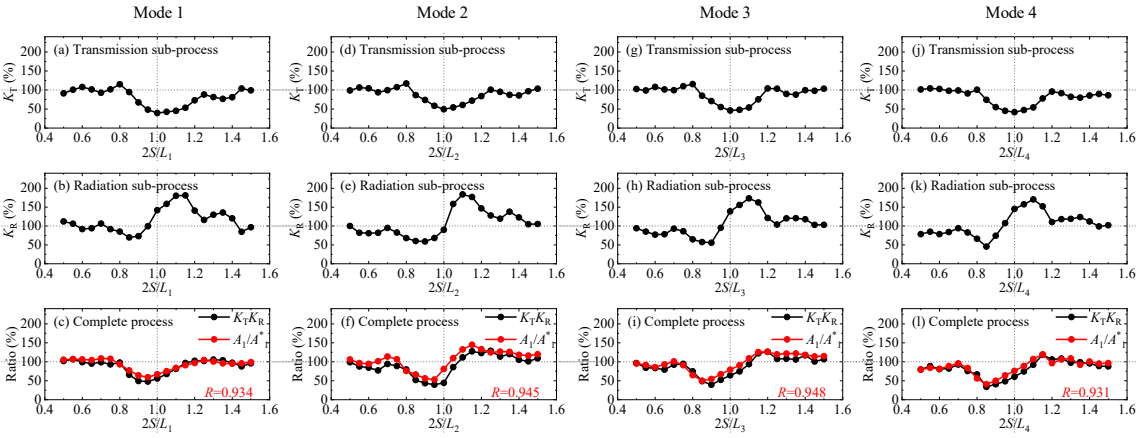

Fig. A2. As in Fig. A1, but for the periodic bars with D/h_0=0.4 and N=4

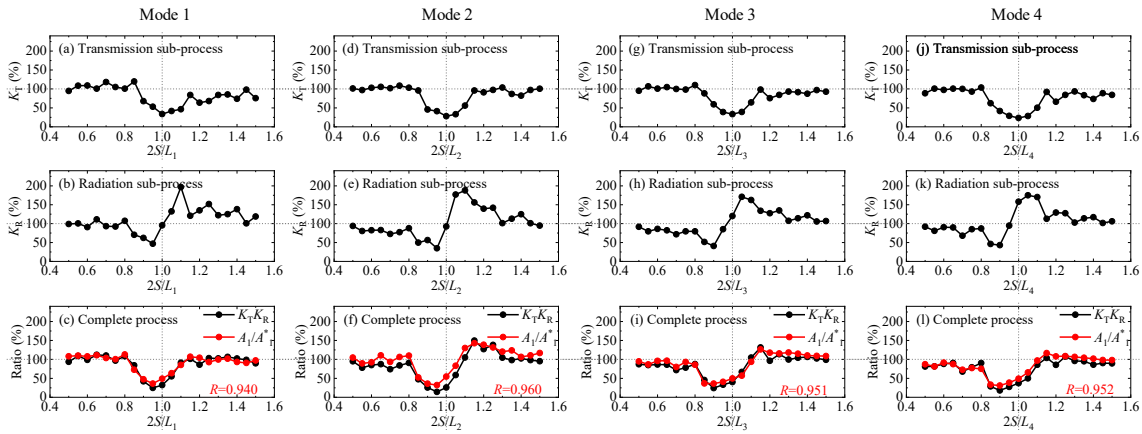

Fig. A3. As in Fig. A1, but for the periodic bars with D/h_0=0.4 and N=6